THE STRUCTURE OF BENZIMIDAZOLE-3-OXIDE-1-OXYL RADICALS IN A TOLUENE
MATRIX : A COMBINED ADVANCED ELECTRON PARAMAGNETIC RESONANCE
SPECTROSCOPY AND QUANTUM MECHANICS CALCULATION STUDY

By

Yo-Yuan Cheng

A THESIS

Submitted to
Michigan State University
in partial fulfillment of the requirements
for the degree of

MASTER OF SCIENCE

Chemistry

2011

ABSTRACT

THE STRUCTURE OF BENZIMIDAZOLE-3-OXIDE-1-OXYL RADICALS IN A TOLUENE
MATRIX : A COMBINED ADVANCED ELECTRON PARAMAGNETIC RESONANCE
SPECTROSCOPY AND QUANTUM MECHANICS CALCULATION STUDY

By

Yo-Yuan Cheng

The present thesis reports the results of a systematic computational and experimental study devoted to a better understanding of magneto-structural relationships in BNNs. From a methodological point of view, the results derived by Barone's PBE0/N07D/PCM model for structural and magnetic properties, which are accurate enough to allow for quantitative studies, are in excellent accord with the information derived from ESEEM and ENDOR and the potential energy surface by UHF-reference QCISD/6-31G*/PCM. We were thus able to unravel the role of different factors (both structural and electronic) in tuning the magnetic properties of nitrogen free radicals.

ACKNOWLEDGMENTS

TABLE OF CONTENTS

LIST OF TABLES

LIST OF FIGURES

Chapter 1

Introduction

Free radicals containing the nitrogen nucleus are present in many processes of chemical, physical, and biological interest. Much of the scientific interest in nitroxide radicals stems from their prominent role as spin labels in biology, biochemistry, biophysics, and nanotechnology to monitor the structure and the motion of macromolecular systems[1, 2]. Indeed, labeling of specific sites by nitroxide probes allows effective structural and dynamic analyses by means of Electron Paramagnetic Resonance (EPR) and Electron-Nuclear Double Resonance (ENDOR) spectroscopy, thanks to the sensitivity of their magnetic parameters (e.g. gyromagnetic and electron-nuclear hyperfine tensors) to interactions with the surrounding molecules and to the polarity of the local environment[3].

Advanced EPR spectroscopy provides rich information consisting essentially of the electron-nuclear hyperfine coupling (A_N) and gyromagnetic (g) tensors. However, interpretation of these experiments in structural terms strongly benefits from quantum mechanical (QM) calculations able to dissect

the overall observables in terms of the interplay of several subtle effects. The computation of nuclear hyperfine tensors by QM methods has a long history, which has finally led to the development of cost-effective and reliable approaches[4-6] [5, 7-14] [15] [16], whereas quantitative calculations of g-tensors for large molecules by the machinery of non-empirical quantum chemistry, have become possible only recently[17] [18].

Free radicals are generally short-lived, highly reactive species, usually characterized experimentally by their magnetic properties only. Thus a successful theoretical approach must be able to provide at the same time reliable structural and magnetic properties. In the past few years, methods based on the unrestricted Kohn-Sham (UKS) approach to density functional theory (DFT) have revolutionized this field, since they couple a remarkable reliability with a very favorable scaling with the number of basis functions, which has become essentially linear in the latest implementations[4, 19]. Furthermore, spin contamination is usually negligible due to a reasonable balance between exchange and correlation contributions. The electron-nuclear hyperfine coupling (A_N) can be factored into both an isotropic (spherically symmetric) and an anisotropic (dipolar) term, $T_{(aniso)}$. The isotropic term (a_{iso}), so called isotropic hyperfine coupling constant (hfcc), depends on the unpaired

electron spin density at the coupled nucleus, making this property very

sensitive to the level of the calculation, specifically to the electron correlation,

the one-electron basis set, and the use of an adequate molecular geometry. In

previous papers[20-24], P. Calle and co-workers investigated the reliability of

the density functional theory (DFT) methodology to compute hfccs of different

nuclei of a large number of both organic and inorganic radicals in their ground

states. The main conclusion was that the best overall results are obtained

when the B3LYP[25, 26] functional is combined with either TZVP[27] or

EPR-III[28, 29] basis sets, yielding highly accurate values of hfccs of nuclei

belonging to the first three rows of the periodic table. An exception was found

for ^{14}N nuclei in which the smaller and less computationally demanding

6-31G* [30, 31] basis set yields hfcc values closer to the experimental ones,

probably due to the fact that it has six d functions instead of the five d functions

of the TZVP and EPR-III basis sets, providing an additional s function to

complete the s space.

Recently, Barone and co-workers developed a new polarized split-valence

basis set for the calculation of hfccs of second- and third-row atoms, the

so-called N07D[32, 33], by adding a reduced number of polarization and

diffuse functions to the 6-31G basis set. To get accurate values of hfccs and

retain, or even improve, the good performance of the parent 6-31G* basis set for other properties dominated by valence orbitals, the new set was tailored by optimizing the core-valence *s* functions and reoptimizing polarization and diffuse *p* functions. Such a basis set was made specifically for both the B3LYP and the parameter-free PBE0[34] functionals.

Here, we adopted Barone's tailored N07D basis set for aromatic systems to evaluate the role of spin delocalization on the geometry and the magnetic parameters by means of DFT computation and advanced EPR spectroscopy. While many studies have been devoted to the comparison between experimental and computed EPR properties of "non-conjugated nitroxides"[7] [5, 35-38], only a few of them deal with aromatic systems[39] [40]. This is quite surprising in view of the remarkable thermal and chemical stability of aromatic nitroxides, in which the –NO spin density is delocalized over the aromatic ring system.

Chapter 2

Materials and Methods

1. Computational details

A good molecular geometry is a mandatory starting point for evaluating the electronic structure. For our study, we used PBE0/N07D/PCM optimized geometries for radicals and compared them with X-ray structures taken from the Cambridge Crystallographic Data Center[41].

2. DFT hyperfine tensor calculation

All quantum mechanical computations were performed with the Gaussian 03 codes[42]. Based on the work of Barone[32], we selected a parameter-free model that was introduced in 1999 (referred to as PBE0)[34]. The redundant set of six d functions has to be employed for the N07D basis set, since it has been developed with this feature[32, 33]. Thus, most of the computations were performed at the PBE0/N07D/PCM level, including full geometry optimizations. The QM calculations were performed in toluene solvent by using the so called polarizable continuum model (PCM) which is a very effective tool for taking into account bulk solvent effects[37, 43].

3. Molecular frame and Euler angles

All calculations were performed by Gaussian03 in the molecular principal

axes (**X**, **Y**, **Z**) defined by the green axes in figure 2.1.
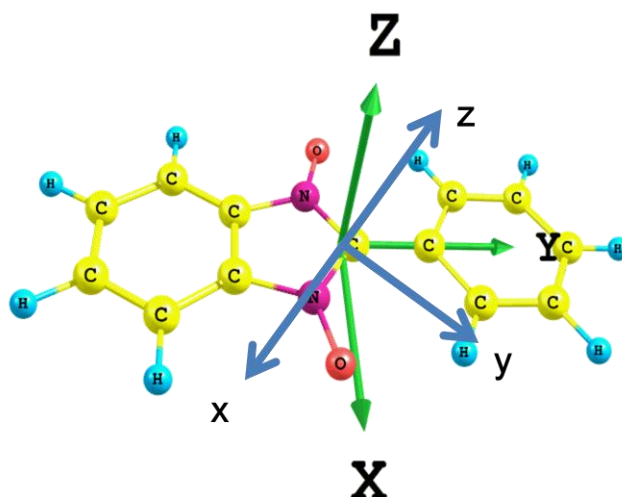
Figure 2.1: Molecular principal axes (X, Y, Z) and the orientation (x, y, z) of each interaction frame (g, A, or Q) For interpretation of the references to color in this and all other figures, the reader is referred to the electronic version of this thesis.

It is customary to specify the orientation of each magnetic interaction with

respect to the principal axis system of the g tensor in an EPR study of frozen

solution samples. For our EPR spectral simulations, we set the g principal axis

frame identical to the molecular principal axes with an identity rotational matrix

for g.

$$g = \begin{bmatrix} 2.012 \\ 2.007 \\ 2.002 \end{bmatrix}$$

$$g.pa = \begin{bmatrix} 1 & 0 & 0 \\ 0 & 1 & 0 \\ 0 & 0 & 1 \end{bmatrix}$$

Therefore, the orientation (x, y, z) of all of the magnetic interactions were

expressed relative to the molecular principal axes. For each interaction (g, A, Q),

a 3x3 orthogonal rotation matrix $R = \begin{bmatrix} R_{11} & R_{12} & R_{13} \\ R_{21} & R_{22} & R_{23} \\ R_{31} & R_{32} & R_{33} \end{bmatrix}$ and 3

"eigenvalues" or principal values $\begin{bmatrix} v_1 \\ v_2 \\ v_3 \end{bmatrix}$ were obtained from Gaussian03. The

set of three Euler angles was determined from the following equations:

$$\alpha = \tan^{-1}\left(\frac{R_{32}}{R_{31}}\right)$$

$$\beta = \tan^{-1}\left(\frac{R_{31}}{R_{33}\cos\alpha}\right) \tag{1}$$

$$\gamma = \tan^{-1}\left(\frac{-R_{23}}{R_{13}}\right)$$

By noting that **R** can be expressed as the product of three non-commutative

rotations α, β, γ about the z, the (new) y and the (new) z axes, respectively:

$$R = R_z(\gamma) \cdot R_y(\beta) \cdot R_z(\alpha)$$

$$= \begin{pmatrix} \cos\gamma & \sin\gamma & 0 \\ -\sin\gamma & \cos\gamma & 0 \\ 0 & 0 & 1 \end{pmatrix} \begin{pmatrix} \cos\beta & 0 & -\sin\beta \\ 0 & 1 & 0 \\ \sin\beta & 1 & \cos\beta \end{pmatrix} \begin{pmatrix} \cos\alpha & \sin\alpha & 0 \\ -\sin\alpha & \cos\alpha & 0 \\ 0 & 0 & 1 \end{pmatrix}$$

$$= \begin{pmatrix} \cos\alpha\cos\beta\cos\gamma - \sin\alpha\sin\gamma & \sin\alpha\cos\beta\sin\gamma + \cos\alpha\cos\gamma & -\sin\beta\cos\gamma \\ -\cos\alpha\cos\beta\cos\gamma - \sin\alpha\sin\gamma & -\sin\alpha\cos\beta\sin\gamma + \cos\alpha\cos\gamma & \sin\beta\sin\gamma \\ \cos\alpha\sin\beta & \sin\alpha\sin\beta & \cos\beta \end{pmatrix}$$

(2)

The Euler rotations in Eq. (2) are defined in a right-handed coordinate system, where a positive angle corresponds to an anticlockwise rotation about the respective axis as viewed looking towards the origin.

4. Sample preparation

Organic radical materials containing unpaired electron spins exhibit technologically useful properties, such as electrical conductivity or ferromagnetism. The goal is to create an assembly of organic molecules or macromolecules made up from only light elements (C, H, O, S, etc.) and possessing properties similar to those of pure metals to enable spin alignment.

Phenylbenzoimidazole-1-yl *N,N*-dioxide (PBIDO)(figure 2.2) is the only benzoimidazole nitroxide radical whose magnetic properties have been reported and it is the only benzoimidazole whose structure has been determined by x-ray crystallography[44]. PBIDO dimerizes and exhibits strong antiferromagnetic coupling. The magnetic properties of these stable radicals, which can be building blocks for new advanced magnetic materials, need to be

explored.
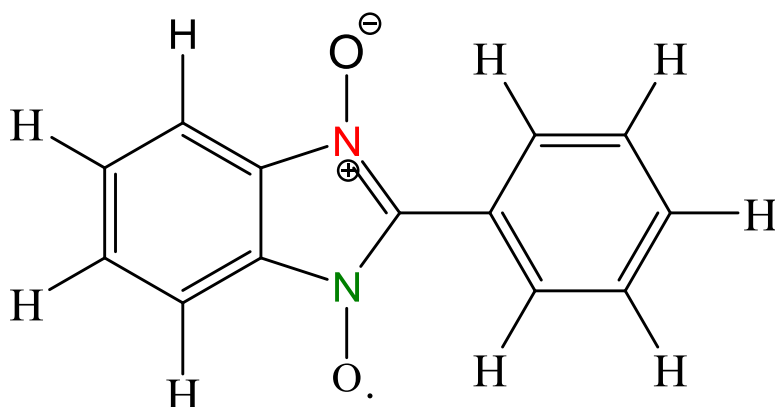
Figure 2.2: PBIDO (BNN radical #1)

We received benzimidazole-3-oxide-1-oxyl radicals (BNNs) (Figure 2.2) from our collaborator, Professor Burak Esat, Department of Chemistry, Fatih University, Turkey. The compounds were dissolved in reagent-grade toluene to a final concentration of 45 mM. A 10-fold molar excess of powdered PbO_2 was then added and the mixture was vortexed for 10 minutes to poise the molecule in its radical form. The resulting solution was centrifuged at high speed to remove excess PbO_2. The radical solution has a yellowish color. A second BNN radical species, where pyridyl replaces the phenyl ring of BNN radical #1 was also studied and labeled as BNN radical #2.

5. Easyspin simulation

Easyspin is a computational package for spectral simulation and analysis in ESEEM and ENDOR[45]. It is based on Matlab, a commercial technical computation software package.

6. ESEEM spectroscopy

Electron Spin Echo Envelope Modulation (ESEEM) spectroscopy became very popular for studying hyperfine and nuclear quadrupole couplings. The application of ESEEM for the measurement of small hyperfine and nuclear quadrupole interactions is described in a number of reviews[46-48]. In this work we used the most widely applied experiment based on the three-pulse, stimulated echo sequence (figure 2.3). ESEEM is one of the few techniques for providing local structure information. In three-pulse ESEEM, an echo envelop modulation is observed when the time delay T between the second and third pulses of a simulated echo sequence is incremented.
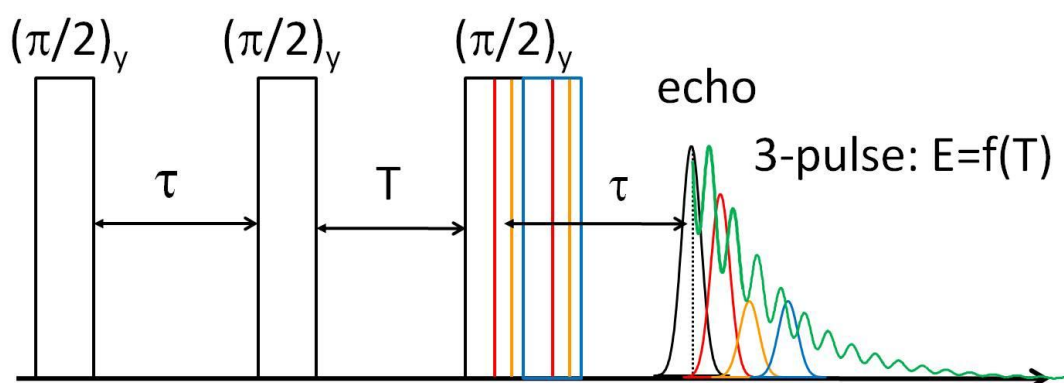
Figure 2.3: In the three-pulse sequence, two pulses separated by time τ are applied, followed by a third pulse after time T, and the stimulated-echo is observed at time τ after the third pulse. The echo envelope is obtained as T is incremented.

7. Advanced EPR instrument

ESEEM and ENDOR data were collected on a Bruker E-680x EPR spectrometer operating at X-(9 GHz) and W-(95 GHz) bands. X-band

experiments used a model EN 4118X-MD4 probe that contained a 4 mm

dielectric resonator. An Oxford model CF-935 liquid helium cryostat and

ITC-503 temperature controller were used to maintain sample temperatures at

10 K for ESEEM and 20 K for ENDOR studies. X-band ESEEM data were

collected using a stimulated echo (90°-τ-90°-T-90°-echo) sequence as

detailed above. A four step phase cycling scheme was used to eliminate

distortions from 2-pulse echoes and correct DC-offsets from the baseline.

ESEEM frequency spectra were obtained from time domain data using a

procedure that involved removal of the "DC+decay" portion of the data,

followed by application of a Hamming window function and then, Fourier

Transformation (FFT). The spectra are then obtained by taking the absolute

value of the FFT output.

8. ENDOR

W-band ENDOR spectra were collected using a Davies ENDOR pulse

sequence with the following parameters; microwave frequency, 9.71 GHz;

microware pulse power, 5 mW; microwave π pulse length, 320 ns; sample

temperature, 20 K; τ-value, 1000 ns; rf (radiowave frequency) pulse width, 800

ns; rf pulse power, 200 W; Spectra were obtained by measuring the amplitude

of the free induction decay (FID) of the radical as function of the applied rf

pulse frequency.

Chapter 3

Theoretical background: EPR

Electron paramagnetic resonance spectroscopy (EPR) is a technique that probes the electronic nature of a paramagnetic species by characterizing the interaction of that species with an applied magnetic field. This method can provide detailed information about the unpaired electron spin density distribution within a paramagnetic species through the measurement of electron-nuclear hyperfine couplings. The magnetic interactions of the systems can be accounted for using a spin Hamiltonian (equation 3), which phenomenologically accounts for all magnetic interactions in the system of interest

$$H = \beta \vec{S} \cdot g \cdot \vec{B} - \beta_n \vec{I} \cdot g_n \cdot \vec{B} + \vec{S} \cdot A \cdot \vec{I} + \vec{I} \cdot \tilde{Q} \cdot \vec{I}$$

(3)

The first term, the electronic Zeeman Hamiltonian, accounts for the interaction between the electron spin and the external magnetic field; $\vec{B}$ is the applied external magnetic field, $\tilde{g}$ is the g-tensor, and β is the electronic Bohr magneton. In general, $\tilde{g}$ can be written as three principal values g_x, g_y, g_z, and three Euler angles (α, β, γ) which describe the orientation of the $\tilde{g}$

principal axes frame relative to the molecular principal axes. For our spectra simulations, the $\tilde{g}$ principal axis frame was considered coincident with the molecular principal axes and all other interaction frames (A and Q) are referred to the molecular principal axes as well.

The hyperfine structure seen in room-temperature CW-EPR experiments arises from electron-nuclear hyperfine coupling (hfc), the third term of equation 3. The magnitude of this interaction is gauged by the hfc tensor, $\tilde{A}$, which collapses to the isotropic hyperfine coupling constant, a_{iso}, in dynamically averaged (i.e. isotropic) conditions (e. g. measured at room temperature). However, hyperfine interactions seen in frozen solution EPR, ESEEM and ENDOR are contributed from both the isotropic hyperfine, a_{iso}, and anisotropic hyperfine interactions, T_{aniso}. The Hamiltonian is represented by

$$H_{HF} = \vec{S} \cdot A \cdot \vec{I} \tag{4}$$

, which comprises one of the most important sources of information in EPR spectroscopy. The hyperfine tensor A can be written as the sum of the isotropic or Fermi contact part and anisotropic part:

$$A = a_{iso}\tilde{1} + T_{aniso} \tag{5}$$

with

$$a_{iso} = \frac{2}{3}\mu_0 g_e g_N \beta_e \beta_N \left|\psi_0(0)\right|^2.$$

$\left|\psi_0(0)\right|^2$ is interpreted as the unpaired electron spin density at the

nucleus.

The anisotropic part can be interpreted in terms of point dipole-dipole

interactions and can be written as

$$T_{aniso} = \frac{\mu_0}{4\pi} g_e g_N \beta_e \beta_N \frac{1}{r^3} \begin{bmatrix} -1 & 0 & 0 \\ 0 & -1 & 0 \\ 0 & 0 & 2 \end{bmatrix}$$

$$= \begin{bmatrix} -T & & \\ & -T & \\ & & 2T \end{bmatrix}$$

(6)

where γ is the distance between the unpaired electron and the interacting

nucleus. ESEEM spectroscopy is a good method to determine these

couplings.

The nuclear Zeeman Interaction

The coupling of a nuclear spin I to the external field B is described by the nuclear Zeeman interaction

$$H_{NZ} = -\beta_N g_N \vec{B} \cdot \tilde{I} \qquad (7)$$

The (isotropic) nuclear g factor, g_N, is an inherent property of a nucleus. For protons the nuclear Zeeman interaction is only 1/658 of the electron Zeeman interaction, for all other nuclei it is even less.

Nuclear quadrupole Interaction

Nuclei with spin I$\geq$1 are distinguished by a non-spherical distribution of protons giving rise to a nuclear electric quadrupole moment Q. The general form of the spin Hamiltonian is

$$H_Q = \vec{I} \cdot Q \cdot \vec{I} \qquad (8)$$

Q is traceless and can be described by:

$$Q = \begin{bmatrix} Q_x & 0 & 0 \\ 0 & Q_y & 0 \\ 0 & 0 & Q_z \end{bmatrix} \qquad (9)$$

The g Tensor Calculation

EPR has played a central role in identifying and characterizing radicals. In this paper, we can learn the calculated g-value of BNN radicals.

The gyromagnetic tensor[49] can be written :

$$g \cong g_e I + \Delta g_{RM} + \Delta g_G + \Delta g_{OZ/SOC}$$ where

g_e is the free-electron value (g_e) 2.0023193 and I is an identity matrix. Computation of the relativistic mass (RM) and gauge (G) corrections is quite straightforward because they are first-order contributions[50]. The last term arises from the coupling of the orbital Zeeman (OZ) and the spin-orbit coupling (SOC) operator. The OZ contribution is computed using the gauge-including atomic orbital (GIAO) approach[51], where for light atoms, the two electron SOC operator can be reliably approximated by a one electron operator involving adjusted effective nuclear charges[28]. Upon complete averaging by rotational motions, only the isotropic part of the g tensor survives, which is given by g_{iso} = 1/3Tr(g). Of course, the corresponding shift from the free electron value is Δg_{iso} = g_{iso} – g_e. All the results will be given as g-tensor values.

PBE0	EPR-II	6-31G*	TZVP	N07D	EPR-III	Exp.
gx	2.013	2.013	2.014	2.013	2.013	2.011
gy	2.007	2.007	2.007	2.007	2.007	2.006
gz	2.002	2.002	2.002	2.002	2.002	2.002

Table 3.1: g tensors calculated by PBE0 functional with different basis sets and experimental results

Chapter 4

Results and Discussion

A prerequisite to electronic structure calculations is the determination of

the optimized geometry of the molecules to be studied. Figure 4.1 shows the

optimized geometry of BNN radical #1 that was obtained by PBE0/N07D/PCM.

The XRD structure of Cambridge Database is also provided for

comparison[41]. These two structures have identical bond length patterns.
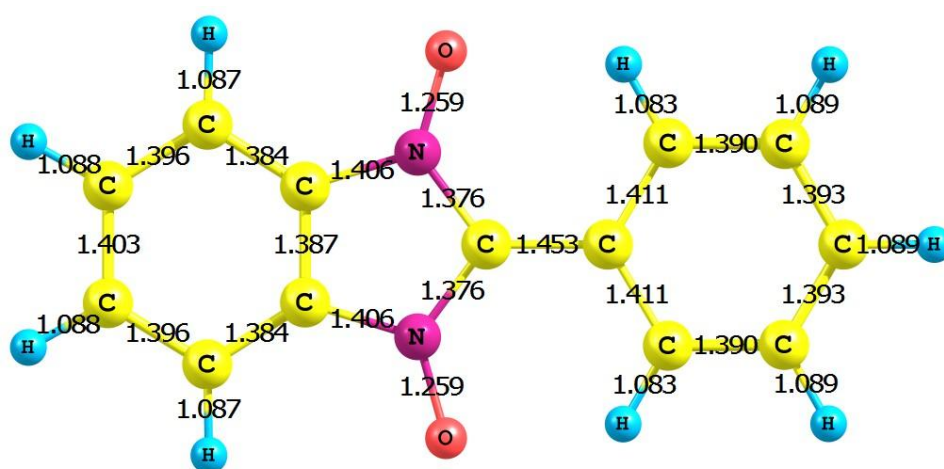
PBE0/N07D/PCM

Figure 4.1: A comparison of the optimized geometry of BNN radical #1 with the XRD
structure[41] Unit: Å

continued figure
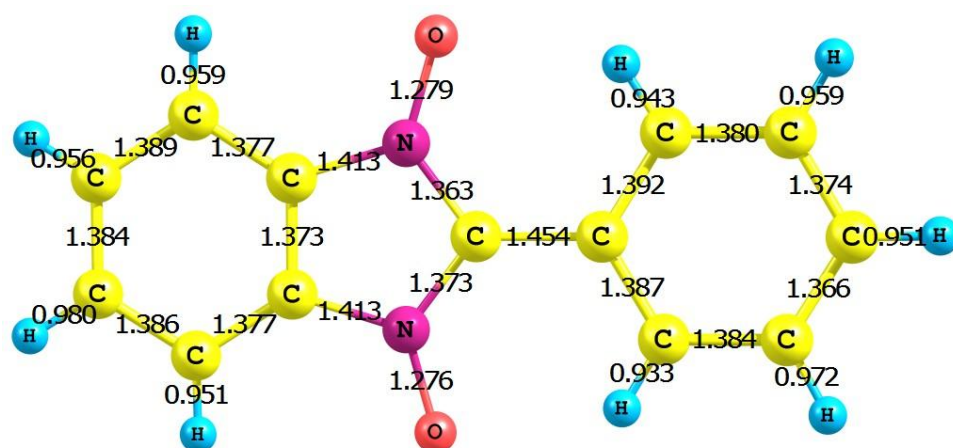
XRD structure

Figure 4.1: A comparison of the optimized geometry of BNN radical #1 with the XRD structure[41] Unit: Å

A continuous wave (CW)–EPR spectrum of BNN radical #1 in toluene is shown in figure 4.2 (red trace). The spectrum shows five absorption peaks with a 1:2:3:2:1 intensity patterns indicative of hyperfine complying to two equivalent ^{14}N nuclei. Because these data were collected at room temperature, only the isotropic portion of the ^{14}N hyperfine couplings is obtained. The ^{14}N isotropic hyperfine coupling (a_{iso}) is 11.2 MHz. The EPR spectrum is centered at an average g-value of 2.006.
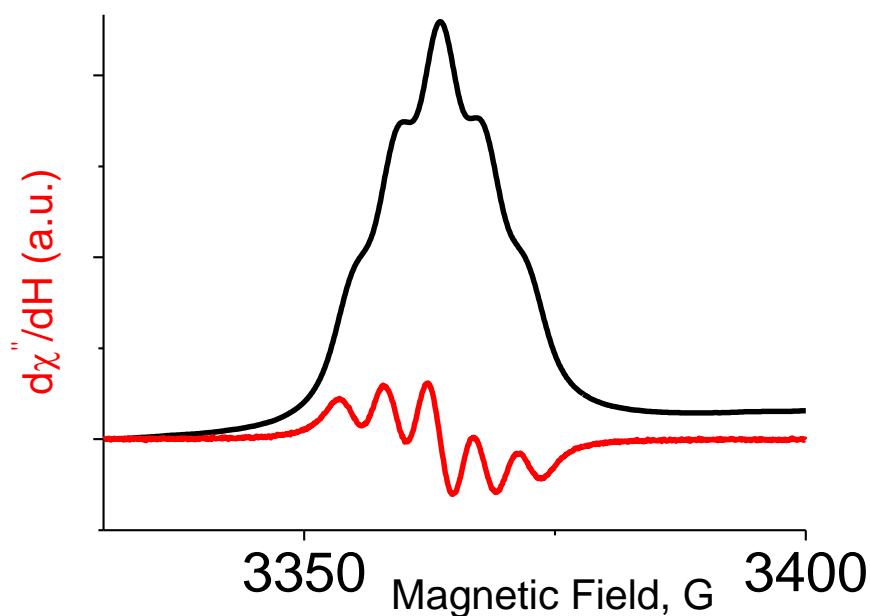
Figure 4.2: CW-EPR spectrum of BNN radical #1 taken at ambient temperature. Condition used to collect the these data were: Microwave frequency: 9.44 GHz. Time constant: 20ms. Conversion time: 80 ms. Modulation frequency: 100 KHz. Modulation amplitude: 1G.

The isotropic hyperfine coupling for the nitrogen atoms of the NO groups can be measured directly from the EPR spectrum of figure 4.2 using the strategy described in the energy level diagram of figure 4.3. The diagram shows the origin of the five EPR transitions resolved in our measurements. The intensity pattern is a consequence of the degeneracy of the hyperfine energy levels.
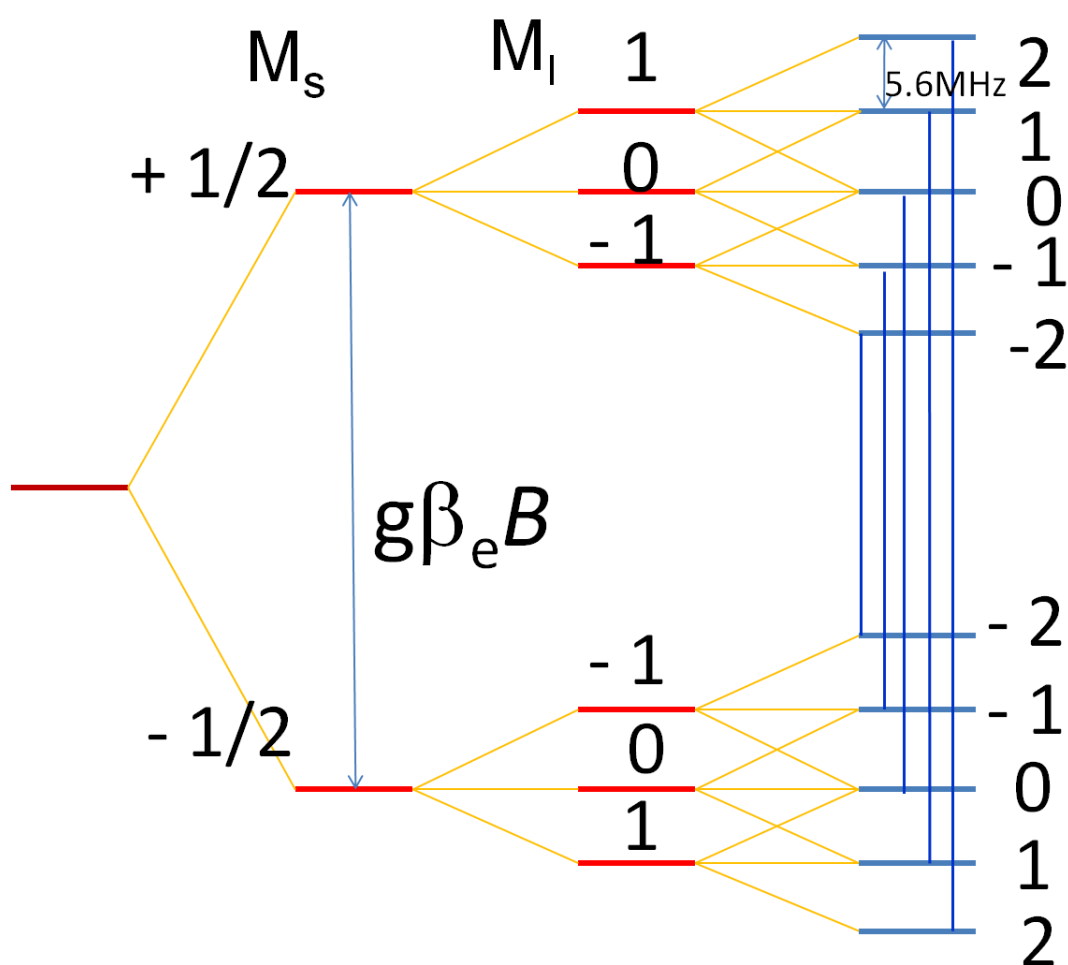
Figure 4.3: Energy levels of a system with one unpaired electron and two identically coupled nuclei with I = 1. At a sufficiently high fixed magnetic field B = 3363 G, the thin line would be the transition corresponding to hv = gβeB in the absence of hyperfine interactions, A. Five absorption peaks can be obtained according to allowed EPR transitions, and the difference of the energy levels is 5.6 MHz.

Figure 4.4 shows an electron spin echo detected EPR spectrum of BNN radical #1 at 94.1 GHz. The data were collected at 20 K with the sample dissolved in deuterated toluene. The high magnetic field required for this experiment led to resolution of the radical's g tensor principal values at the magnetic field positions marked with arrows. The measured g values are g_x =

2.011, g_y = 2.006, and g_z = 2.002. Because the high field g-value is near the

free electron g value, it is assigned to the direction along the $2p_\pi$ or $2p_z$ orbital

on the nitrogen of the NO groups. These data also show ^{14}N hyperfine splitting

associated with the g_z = 2.002 feature of the spectrum and thus, provides a

direct measurement of the z-component for the ^{14}N hyperfine coupling, A_z =

35.6 MHz. The g_x and g_y features of the spectrum are narrow indicating that

the ^{14}N hyperfine couplings in the plane of the molecule are small.
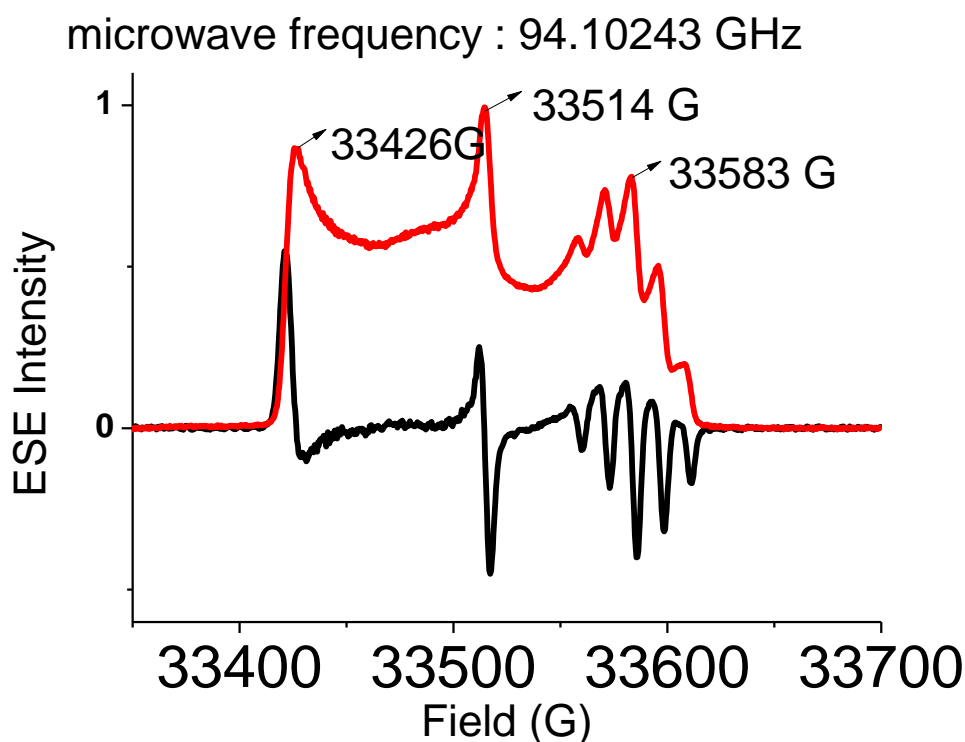
Figure 4.4: Field-Swept, echo-detected EPR spectrum at W-band (microwave
frequency: 94.1 GHz) of 180mM BNN radical #1 in D-toluene at 20 K. Because the
sample is a frozen solution, the anisotropies in the electronic Zeeman and [14]N

hyperfine interaction are revealed. The measured g-value are g_x = 2.011, g_y = 2.006,

and g_z = 2.002. The five absorption pattern centered at g_z =2.002 shows the intensity

pattern, 1:2:3:2:1, and can be assigned to the [14]N's of the 2 N-O groups. The

anisotropic hyperfine interaction at g_z (A_z) is 35.6 MHz. The pulse sequence is

$$\pi/2 - \tau - \pi - \tau - echo \text{, with } t_{\pi/2} = 160 \text{ ns, } t_{\pi} = 320 \text{ ns, and } \tau = 1000 \text{ ns.}$$

Taken together, the X-band solution spectrum and the W-band frozen solution spectrum provide sufficient information to estimate the principal values of the ^{14}N hyperfine tensors for BNN radical #1. If we take the coupling to be the sum of a scalar, isotropic component and a traceless anisotropic portion of axial symmetry, thus $A_x = A_y = a_{iso} - T$ while $A_z = a_{iso} + 2T$. Placing the measured a_{iso} and A_z values into the latter expression, an estimated value of T = 12.2 MHz is obtained. If the nitronyl nitrogen hyperfine coupling is axial, then $A_x = A_y = $ -1.0 MHz. This small value is in agreement with the lack of ^{14}N-hyperfine splitting for the two lower field g features of the W-band spectrum (figure 4.4).

$$A = \begin{pmatrix} a_{iso} & & \\ & a_{iso} & \\ & & a_{iso} \end{pmatrix} + \begin{pmatrix} -T & & \\ & -T & \\ & & 2T \end{pmatrix}$$

$$= \begin{pmatrix} 11.2 & & \\ & 11.2 & \\ & & 11.2 \end{pmatrix} + \begin{pmatrix} -T & & \\ & -T & \\ & & 2T \end{pmatrix} = \begin{pmatrix} A_x & & \\ & A_y & \\ & & 35.6 \end{pmatrix}$$

$$T = 12.2\,MHz$$
$$A_x = A_y = -1.0\,MHz$$

$$A = \begin{bmatrix} A_x & & \\ & A_y & \\ & & A_z \end{bmatrix} = \begin{bmatrix} a_{iso} - T(1+\eta) & 0 & 0 \\ 0 & a_{iso} - T(1-\eta) & 0 \\ 0 & 0 & a_{iso} + 2T \end{bmatrix}$$

How to determine η ?
ESEEM

Figure 4.5: From room-temperature X-band CW-EPR spectrum of BNN radical #1, we can get the isotropic hyperfine couplings (a_{iso}), which are 11.2 MHz. From W-band frozen solution field swept at 20 K, we can get A_z = 35.6 MHz. A_x and A_y are approximately -1.0 MHz.

ESEEM spectroscopy at X-band offers the best chance to measure weak

[14]N hyperfine couplings like those predicted for A_x and A_y of BNN radical #1.

Figure 4.6 shows X-band 3-pulse ESEEM data collected for the radical at 3456

G, g = 2.006. The ESEEM spectrum shows a broad peak centered at 2.6 MHz

with a shoulder at 1.6 MHz and a broad, less intense peak at 4.5 MHz. ESEEM

spectra similar to these have been reported for the semiquinone catalytic

intermediate of copper amine oxidases[52]. For that system, the nitrogen

nucleus that gave rise to the ESEEM was also from a heterocyclic π-radical

where the perpendicular hyperfine component was found to be at low

frequency.

(a)
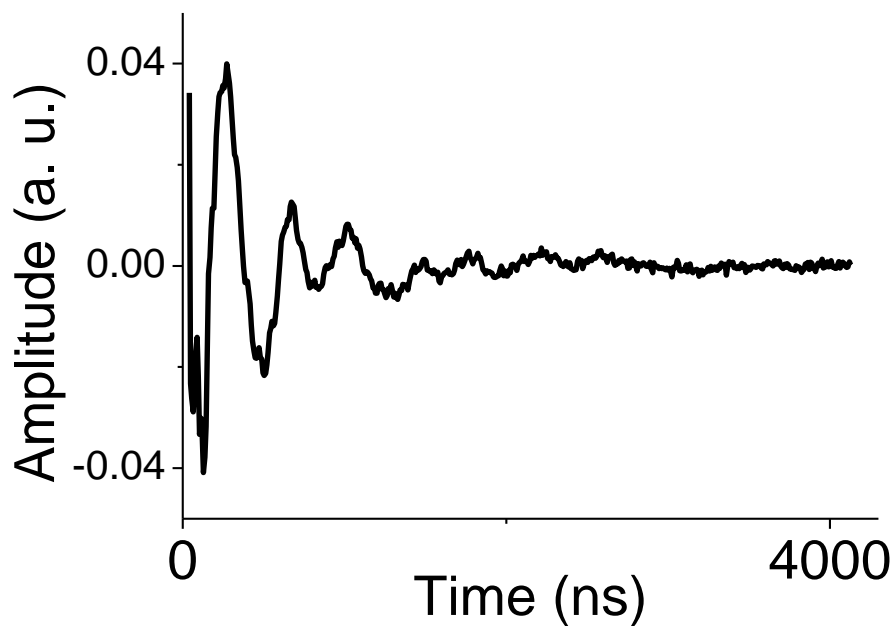
Figure 4.6: Figure (a) shows time domain ESEEM data of the BNN radical #1. Figure (b) shows the Fourier transformations of the respective time domain traces to (a). Spectrometer conditions: magnetic field strength, 3465 G; microwave frequency, 9.729 GHz; microwave pulse power, 54 dBm; sample temperature, 10.0 K; τ value, (a) and (b) 136 ns; starting T value, (a) and (b) 40 ns; time increment, 8 ns.

continued figure

(b)
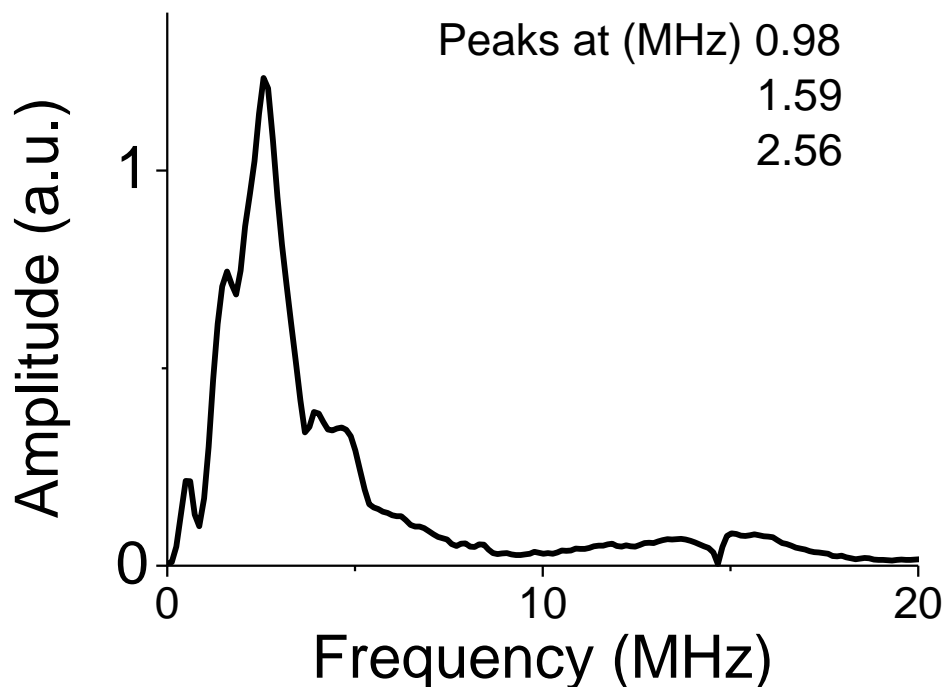
Figure 4.6: Figure (a) shows time domain ESEEM data of the BNN radical #1. Figure (b) shows the Fourier transformations of the respective time domain traces to (a). Spectrometer conditions: magnetic field strength, 3465 G; microwave frequency, 9.729 GHz; microwave pulse power, 54 dBm; sample temperature, 10.0 K; τ value, (a) and (b) 136 ns; starting T value, (a) and (b) 40 ns; time increment, 8 ns.

^{14}N hyperfine coupling analysis

To analyze the ^{14}N ESEEM spectrum shown in figure 4.6, we need the following parameters : g_n, the ^{14}N nuclear g-value; A_x, A_y, A_z, the three ^{14}N electron-nuclear hyperfine coupling principal values;

$\left\{ A_{pa}\alpha, A_{pa}\beta, A_{pa}\gamma \right\}$, the three Euler angles that describe the orientation of the electron-nuclear hyperfine principal axis relative to molecular

principal axes; Q_x, Q_y, Q_z, the three nuclear quadrupole interaction principal

values; $\left\{ Q_{pa}\alpha, Q_{pa}\beta, Q_{pa}\gamma \right\}$, the three Euler angles describing the orientation of

the nuclear quadrupole principal axes relative to molecular principal axes.

To facilitate the analysis, we performed DFT calculations on BNN radical

#1. Our goal was to gain theoretical predictions of the perpendicular ^{14}N

hyperfine couplings, A_x, A_y, and the parameters that describe the ^{14}N nuclear

quadrupole interaction. The orientations of the principal axis system of these

interactions are also needed for ESEEM simulations, and supplied by the DFT

calculations. As mentioned above, our spectral simulations were done with the

program, Easyspin. Fortunately, the common axis systems to which all

magnetic interactions are placed for calculation in Easyspin, is the molecular

axis system. Parameters calculated with Gaussian03 are also referenced to

the molecular axis system. This allowed us to use the Gaussian03 parameters

directly in our simulations.

Gaussian03 input setup

Gaussian03 calculations were performed using the optimized geometry

for BNN radical #1 showed in figure 4.1 and the molecular axis system

depicted in figure 4.7. The basis sets used with the PBE0 functional were

EPR-II, EPR-III, N07D, TZVP, and 6-31G*. Solvent effects were modeled with

PCM. For each basis set, we calculated the hyperfine coupling principal values,

the Euler angles describing the orientation of the hyperfine coupling (principal)

axes relative to the molecular (principal) axes, the nuclear quadrupole coupling

principal values, and the Euler angles of nuclear quadrupole (principal) axes

relative to molecular (principal) axes. During the course of the study, we found

that the dihedral angle that describes the orientation of the phenyl ring relative

to the plane of the benzoimidazole group (figure 4.7), has a modest affect on

the nitrogen coupling for the NO groups, while these conformational effects

were too small to influence the ^{14}N-ESEEM, they did affect the ^{1}H couplings of

the phenyl ring measured by ENDOR and discussed later in this thesis.
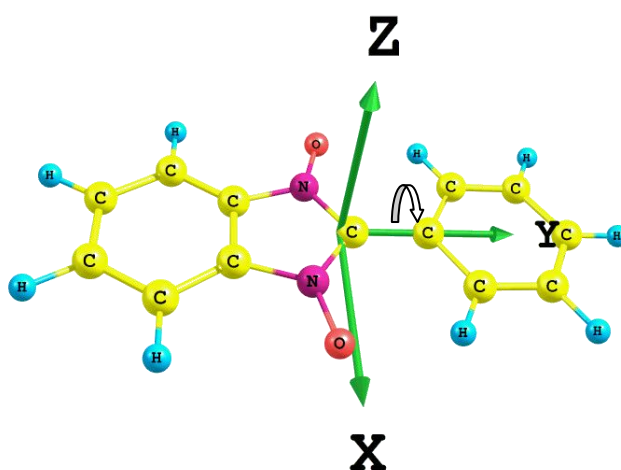
Figure 4.7: Different dihedral angles of the phenyl ring of BNN radical #1 are calculated in Gaussian03 by PBE0/EPR-II (or EPR-III, N07D, TZVP, and 6-31G*)/PCM.

Table 4.1-4.5 on the following pages show the results of our DFT

calculations using the different basis sets listed above with the PBE0 functional.

Two sets of ^{14}N hyperfine and nuclear quadrupole interaction parameters are

given, one for each of the NO nitrogens. The electron-nuclear hyperfine

couplings are given in MHz and the Euler angles are in radians. Each of these

tables is followed by a set of corresponding ^{14}N-ESEEM simulations. The

simulations are displayed in red and provided as a function of the dihedral

angle describing the phenyl group orientations (figure 4.7).

Overall, the most satisfactory simulations as judged by the predicted

ESEEM frequencies and relative amplitudes resulted from parameters

dervived from use of the EPR-III (figure 4.9) and N07D (figure 4.10) basis sets.

At first glance, the N07D parameters appear to do a worse job than those of

the EPR-III basis set because they predicted a frequency component at 0.5

MHz that is not observed in our experiments (figure 4.10b-black trace vs. red

trace). However, part of the processing of ESEEM data calls for the removal of

the function background decay and this always distorts the low frequency

portion of the spectrum if the modulated part of the data is strongly damped.

The time domain ^{14}N ESEEM data shown in figure 4.6a show that the ^{14}N

modulation is weak in that the initial modulation amplitude is only about 8 % of

the signal strength and that these amplitudes are < 1% after the pulse spacing

T > 1μ second. No attempt was made to model signal damping in our

simulations and this could easily account for the discrepancy observed at low

frequency for the simulations derived from the N07D basis set. The simulated

^{14}N ESEEM parameters for these two basis sets at a phenyl ring dihedral

angle of 40-45° are given in table 4.6.

The Euler angles associated with orienting the principal axis systems of

the nuclear quadrupole interactions with respect to the molecular axes show

that the directions of the strongest interaction for both NO nitrogens is aligned

with the molecular z-axis or the 2p$_\pi$ orbital. The interplay between the α and γ

angles is such that the Q_x component is turned ±15.5^o from the molecular

frame x-axis bringing it in line with the NO bond directions for each interaction.

The Euler angles associated with the electron-nuclear hyperfine principal axis

system show that its z-axis is also aligned with the 2p$_\pi$ orbital on the NO

nitrogens coincident with the molecular z-axis. In the plane of molecule, the

x-axis of the hyperfine tensor is rotated ± 90° from the molecular frame to the

NO groups.

EPRII	0D	42D	45D	90D
a_{iso}(MHz)	9.69	9.60	9.59	9.32
a_{iso1}	9.69	9.60	9.59	9.33
T_{xx}(MHz)	-11.72	-11.44	-11.41	-11.22
T_{yy}	-10.69	-10.42	-10.40	-10.18
T_{zz}	22.41	21.86	21.81	21.40
T_{xx1}	-11.72	-11.44	-11.41	-11.22
T_{yy1}	-10.69	-10.42	-10.40	-10.18
T_{zz1}	22.41	21.86	21.81	21.40
Q_{xx}(a.u.)	-0.42	-0.40	-0.40	-0.39
Q_{yy}	-0.07	-0.06	-0.06	-0.05
Q_{zz}	0.49	0.47	0.46	0.44
Q_{xx1}	-0.42	-0.40	-0.40	-0.39
Q_{yy1}	-0.07	-0.06	-0.06	-0.05
Q_{zz1}	0.49	0.47	0.46	0.44
$A_{\cdot pa}\alpha$ (rad)	1.57	0.28	0.28	0.28

Table 4.1: Nitrogen parameter table obtained from Gaussian03 (PBE0/EPR-II/PCM) with different phenyl ring dihedral angles (degree, D) Note : Quadrupole hyperfine couplings in MH were obtained by multiplying the EFG in a. u. by the nuclear electric quadrupole moment (in b) times 234.9647 and divided by 2I(2I-1)[53]. Q (^{14}N) :

0.02044 b. e^2Qq = EFG * 0.02044*234.9647 in MHz ; $\eta = \dfrac{Q_{xx} - Q_{yy}}{Q_{zz}}$

continued table

A.$_{pa}\beta$	0.00	0.00	0.00	0.00
A.$_{pa}\gamma$	0.00	1.29	1.29	1.29
A.$_{pa1}\alpha$	-1.57	-0.28	-0.28	-0.28
A.$_{pa1}\beta$	0.00	0.00	0.00	0.00
A.$_{pa1}\gamma$	0.00	-1.29	-1.29	-1.29
Q.$_{pa}\alpha$(rad)	0.00	1.25	1.25	0.00
Q.$_{pa}\beta$	0.00	0.03	-0.03	0.00
Q.$_{pa}\gamma$	0.00	-0.98	-0.98	0.00
Q.$_{pa1}\alpha$	0.00	-1.25	-1.25	0.00
Q.$_{pa1}\beta$	0.00	0.03	-0.03	0.00
Q.$_{pa1}\gamma$	0.00	0.98	0.98	0.00

Table 4.1: Nitrogen parameter table obtained from Gaussian03 (PBE0/EPR-II/PCM) with different phenyl ring dihedral angles (degree, D)

Note : Quadrupole hyperfine couplings in MH were obtained by multiplying the EFG in a. u. by the nuclear electric quadrupole moment (in b) times 234.9647 and divided by 2I(2I-1)[53]. Q (^{14}N) : 0.02044 b. e^2Qq = EFG * 0.02044*234.9647 in MHz ;

$$\eta = \frac{Q_{xx} - Q_{yy}}{Q_{zz}}$$

(a)
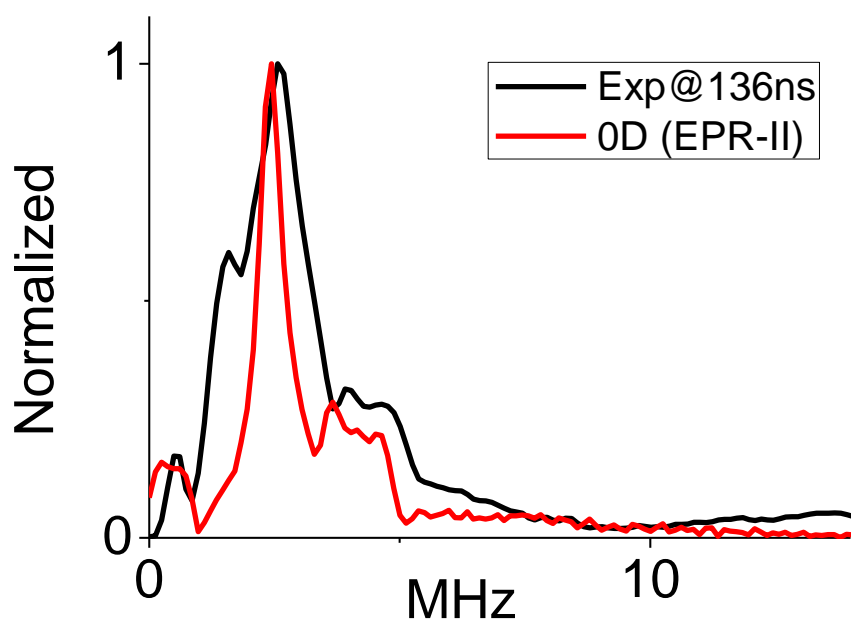
(b)

Figure 4.8 (a-c): Easyspin simulations by the parameters obtained from PBE0/EPR-II /PCM calculation of different phenyl dihedral angles on BNN radical #1 and ESEEM spectrum obtained from Bruker E680 at 10 K

figure continued

(c)

Figure 4.8 (a-c): Easyspin simulations by the parameters obtained from PBE0/EPR-II /PCM calculation of different phenyl dihedral angles on BNN radical #1 and ESEEM spectrum obtained from Bruker E680 at 10 K

EPR-III	00D	40D	90D
a_{iso}(MHz)	10.01	9.91	9.69
a_{iso1}	10.01	9.91	9.69
T_{xx}(MHz)	-12.33	-12.03	-11.81
T_{yy}	-11.39	-11.11	-10.87
T_{zz}	23.72	23.15	22.68
T_{xx1}	-12.33	-12.03	-11.81
T_{yy1}	-11.39	-11.11	-10.87
T_{zz1}	23.72	23.15	22.68
Q_{xx}(a.u.)	-0.38	-0.36	-0.35
Q_{yy}	-0.03	-0.02	-0.01
Q_{zz}	0.41	0.39	0.35
Q_{xx1}	-0.38	-0.36	-0.35
Q_{yy1}	-0.03	-0.02	-0.01
Q_{zz1}	0.41	0.39	0.35
$A_{.pa}\alpha$ (rad)	1.57	0.28	0.28
$A_{.pa}\beta$	0.00	0.00	0.00
$A_{.pa}\gamma$	0.00	1.29	1.29

Table 4.2: Nitrogen parameter table obtained from Gaussian03 (PBE0/EPR-III/PCM)

with different phenyl ring dihedral angles (degree, D)

continued table

$A_{pa1}\alpha$	-1.57	-0.28	-0.28
$A_{pa1}\beta$	0.00	0.00	0.00
$A_{pa1}\gamma$	0.00	-1.29	-1.29
$Q_{Pa}\alpha(rad)$	0.00	1.25	0.00
$Q_{pa}\beta$	0.00	0.03	0.00
$Q_{pa}\gamma$	0.00	-0.98	0.00
$Q_{pa1}\alpha$	0.00	-1.25	0.00
$Q_{pa1}\beta$	0.00	0.03	0.00
$Q_{pa1}\gamma$	0.00	0.98	0.00

Table 4.2: Nitrogen parameter table obtained from Gaussian03 (PBE0/EPR-III/PCM) with different phenyl ring dihedral angles (degree, D)

(a)
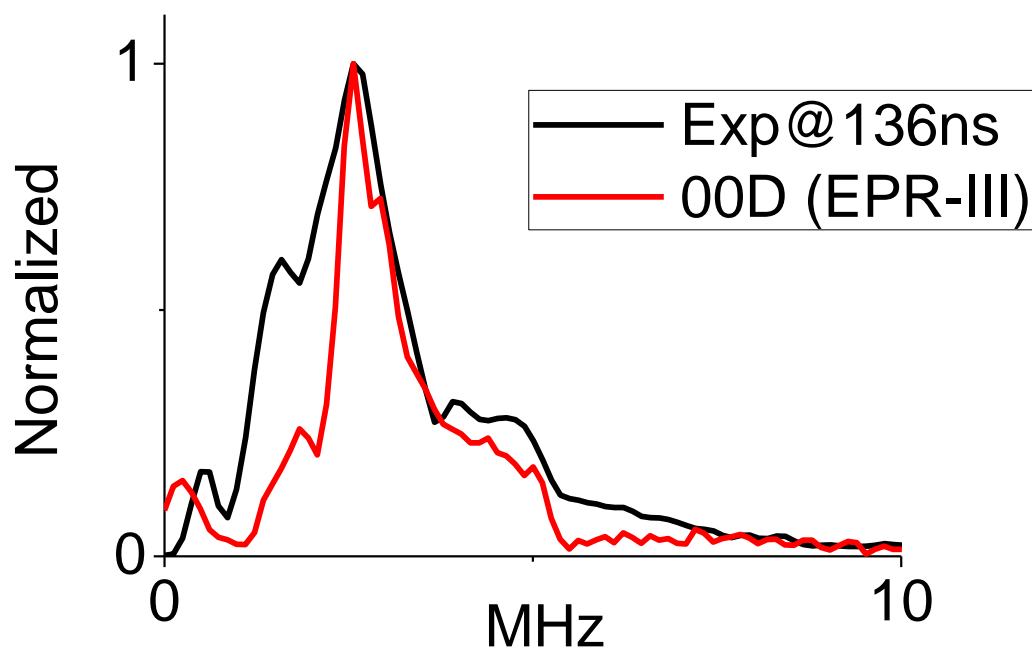
(b)

Figure 4.9 (a-c): Easyspin simulations with the parameters obtained from PBE0/EPR-III/PCM calculation of different phenyl dihedral angles on BNN radical #1 and ESEEM spectrum obtained from Bruker E680 at 10 K
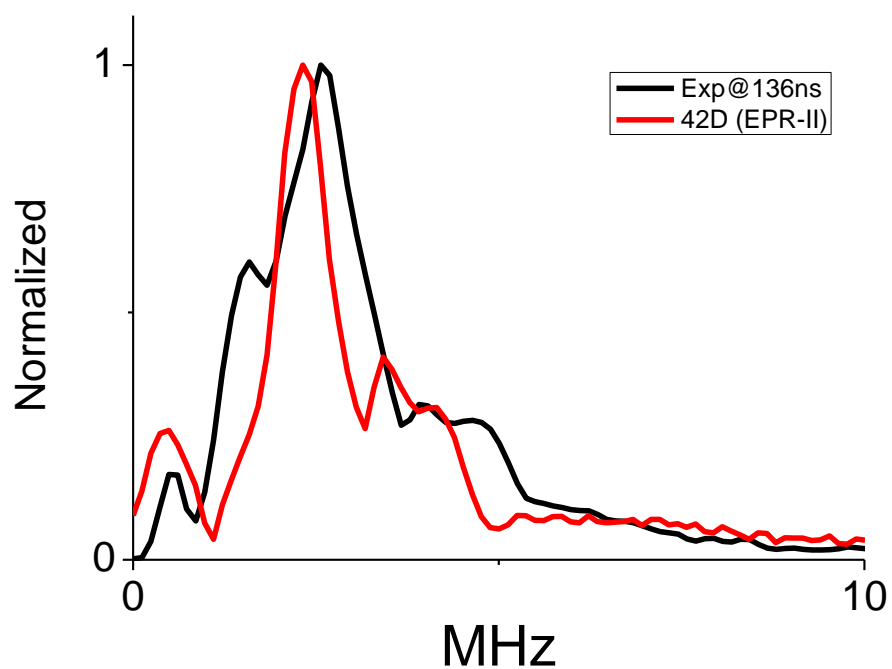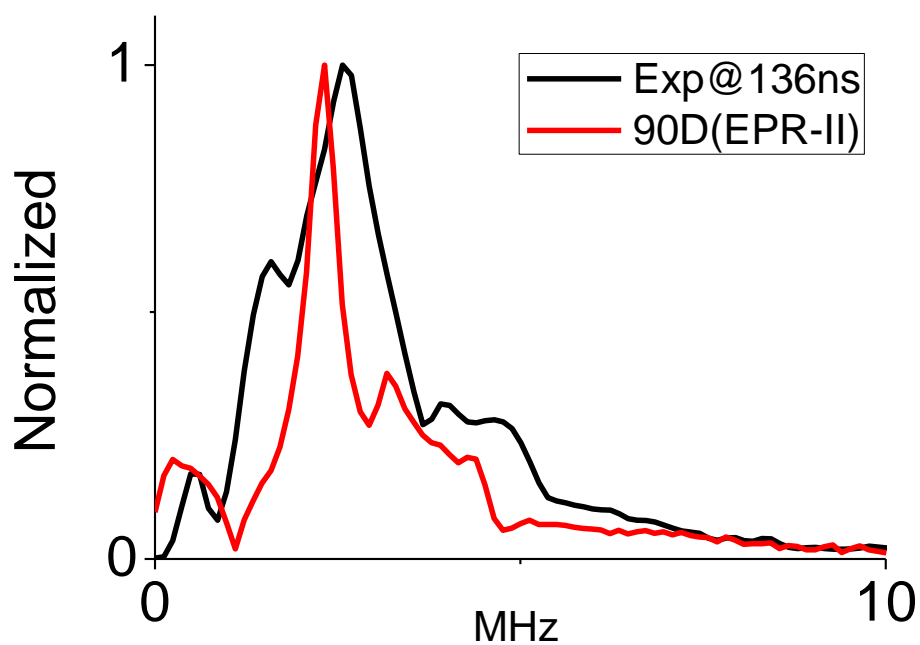
figure continued

(c)

Figure 4.9 (a-c): Easyspin simulations with the parameters obtained from PBE0/EPR-III/PCM calculation of different phenyl dihedral angles on BNN radical #1 and ESEEM spectrum obtained from Bruker E680 at 10 K

N07D	00D	45D	90D
a_{iso}(MHz)	11.79	11.60	11.35
$a_{iso}1$	11.79	11.60	11.36
T_{xx}(MHz)	-11.30	-10.97	-10.80
T_{yy}	-10.22	-9.90	-9.71
T_{zz}	21.51	20.88	20.51
$T_{xx}1$	-11.30	-10.97	-10.80
$T_{yy}1$	-10.22	-9.90	-9.72
$T_{zz}1$	21.51	20.88	20.52
Q_{xx}(a.u.)	-0.37	-0.35	-0.33
Q_{yy}	-0.06	-0.05	-0.03
Q_{zz}	0.43	0.39	0.37
$Q_{xx}1$	-0.37	-0.35	-0.33
$Q_{yy}1$	-0.06	-0.05	-0.03
$Q_{zz}1$	0.43	0.39	0.37

Table 4.3: Nitrogen parameter table obtained from Gaussian03 (PBE0/N07D/PCM) with different phenyl ring dihedral angles (degree, D)

continued table

$A_{.pa}\alpha$ (rad)	1.57	0.28	0.28
$A_{.pa}\beta$	0.00	0.00	0.00
$A_{.pa}\gamma$	0.00	1.29	1.29
$A_{.pa1}\alpha$	-1.57	-0.28	-0.28
$A_{.pa1}\beta$	0.00	0.00	0.00
$A_{.pa1}\gamma$	0.00	-1.29	-1.29
$Q_{.pa}\alpha$(rad)	0.00	1.25	1.25
$Q_{.pa}\beta$	0.00	-0.03	0.03
$Q_{.pa}\gamma$	0.00	-0.98	-0.98
$Q_{.pa1}\alpha$	0.00	-1.25	1.25
$Q_{.pa1}\beta$	0.00	-0.03	0.03
$Q_{.pa1}\gamma$	0.00	0.98	-0.98

Table 4.3: Nitrogen parameter table obtained from Gaussian03 (PBE0/N07D/PCM) with different phenyl ring dihedral angles (degree, D)

(a)
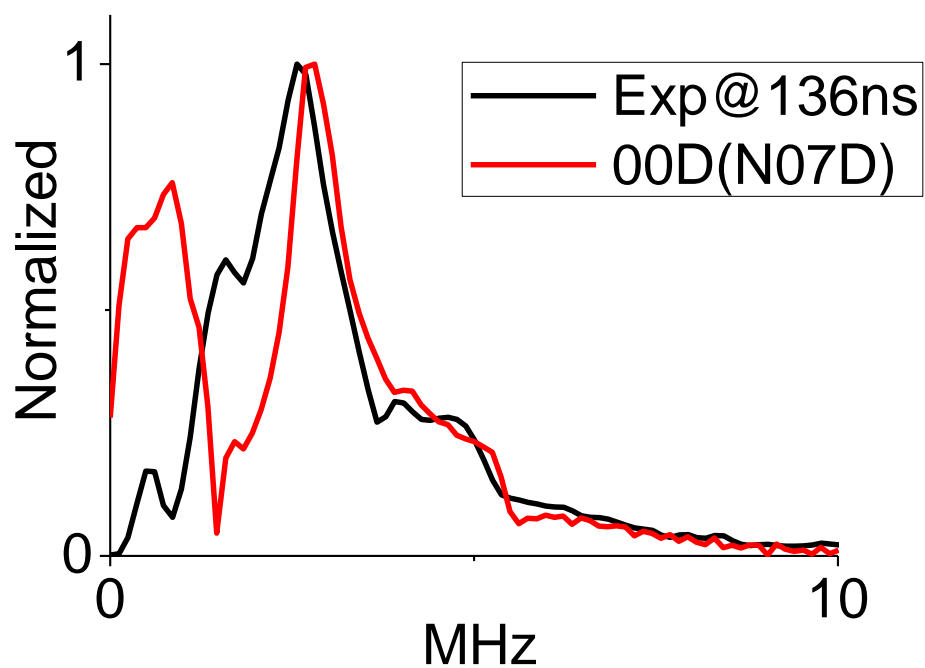
(b)

Figure 4.10 (a-c): Easyspin simulations by the parameters obtained from PBE0/N07D/ PCM calculation of different phenyl dihedral angles on BNN radical #1 and ESEEM spectrum obtained from Bruker E680 at 10 K
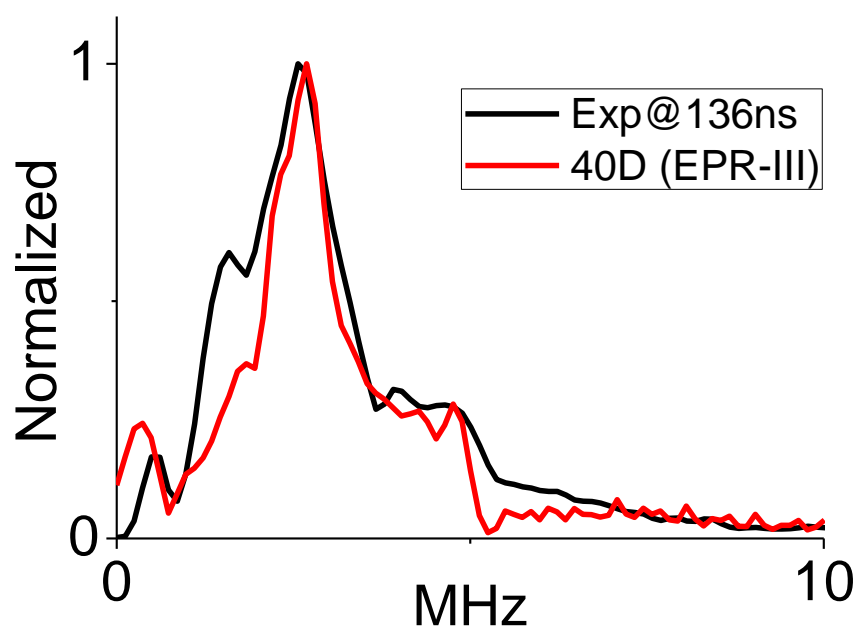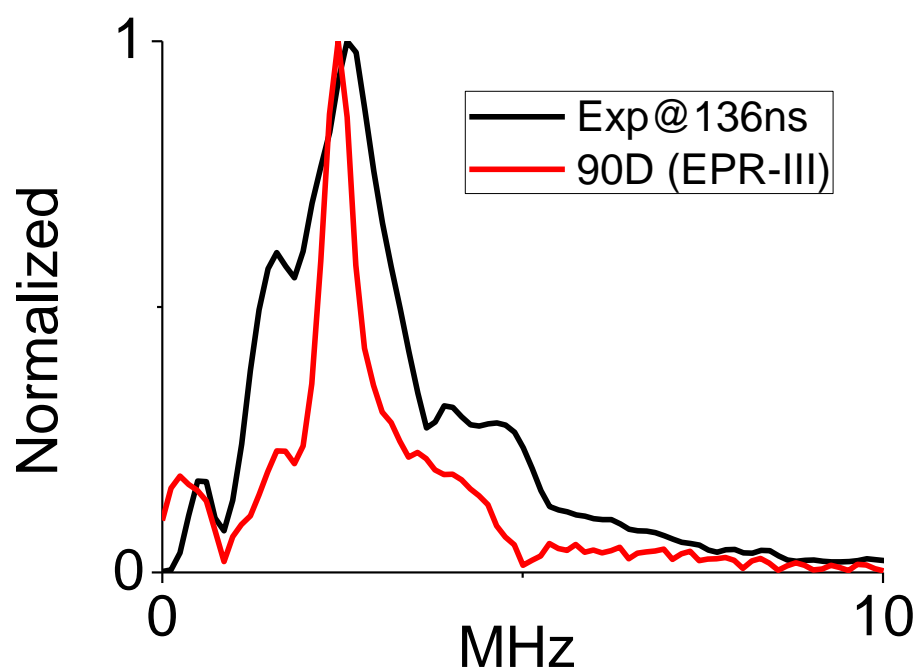
figure continued

(c)

Figure 4.10 (a-c): Easyspin simulations by the parameters obtained from PBE0/N07D/ PCM calculation of different phenyl dihedral angles on BNN radical #1 and ESEEM spectrum obtained from Bruker E680 at 10 K

| TZVP	00D	42D	90D
a_{iso}(MHz)	8.88	8.79	8.56
a_{iso1}	8.88	8.78	8.56
T_{xx}(MHz)	-11.94	-11.62	-11.38
T_{yy}	-10.89	-10.58	-10.33
T_{zz}	22.84	22.20	21.71
T_{xx1}	-11.94	-11.62	-11.39
T_{yy1}	-10.89	-10.58	-10.33
T_{zz1}	22.83	22.20	21.71
Q_{xx}(a.u.)	-0.39	-0.37	-0.36
Q_{yy}	-0.04	-0.03	-0.01
Q_{zz}	0.43	0.40	0.37
Q_{xx1}	-0.39	-0.37	-0.36
Q_{yy1}	-0.04	-0.03	-0.01
Q_{zz1}	0.43	0.40	0.37

Table 4.4: Nitrogen parameter table obtained from Gaussian03 (PBE0/TZVP/PCM) with different phenyl ring dihedral angles (degree, D)

continued table

$A_{\cdot pa}\alpha$ (rad)	1.57	0.28	0.28
$A_{\cdot pa}\beta$	0.00	0.00	0.00
$A_{\cdot pa}\gamma$	0.00	1.29	1.29
$A_{\cdot pa1}\alpha$	-1.57	-0.28	-0.28
$A_{\cdot pa1}\beta$	0.00	0.00	0.00
$A_{\cdot pa1}\gamma$	0.00	-1.29	-1.29
$Q_{\cdot pa}\alpha$(rad)	0.00	1.25	0.00
$Q_{\cdot pa}\beta$	0.00	0.03	0.00
$Q_{\cdot pa}\gamma$	0.00	-0.98	0.00
$Q_{\cdot pa1}\alpha$	0.00	-1.25	0.00
$Q_{\cdot pa1}\beta$	0.00	0.03	0.00
$Q_{\cdot pa1}\gamma$	0.00	0.98	0.00

Table 4.4: Nitrogen parameter table obtained from Gaussian03 (PBE0/TZVP/PCM) with different phenyl ring dihedral angles (degree, D)

(a)
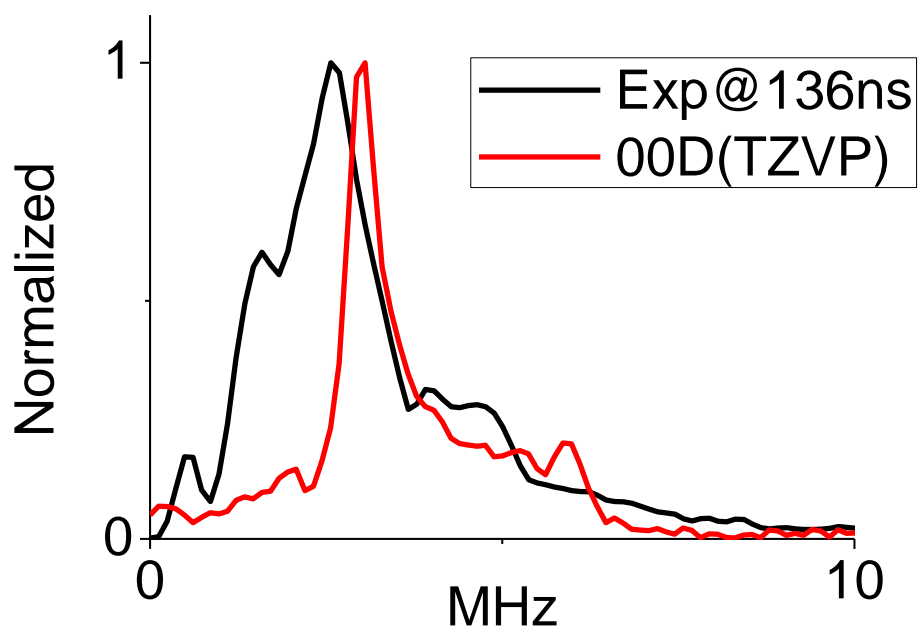
(b)

Figure 4.11(a-c): Easyspin simulations by the parameters obtained from PBE0/TZVP /PCM calculation of different phenyl dihedral angles on BNN radical #1 and ESEEM spectrum obtained from Bruker E680 at 10 K
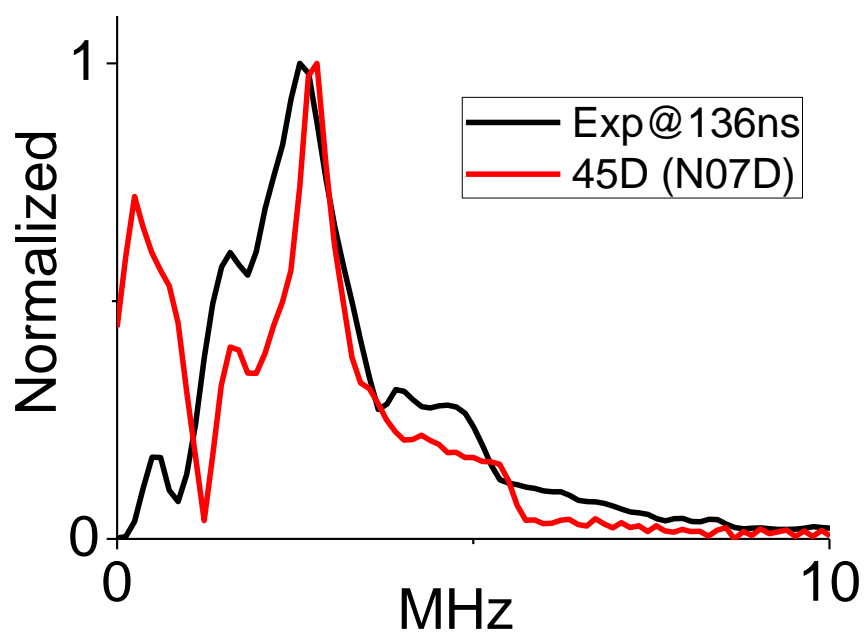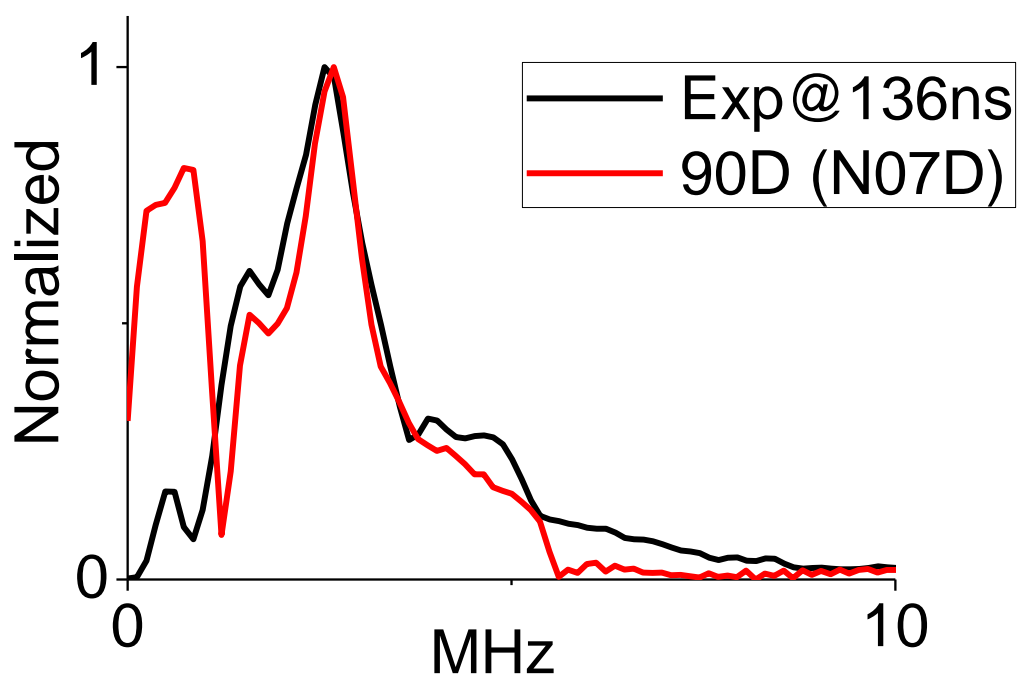
continued figure

(c)

Figure 4.11(a-c): Easyspin simulations by the parameters obtained from PBE0/TZVP /PCM calculation of different phenyl dihedral angles on BNN radical #1 and ESEEM spectrum obtained from Bruker E680 at 10 K

| 6-31G*	0D	42D	90D
a_{iso}(MHz)	11.83	11.57	11.15
a_{iso1}	11.83	11.57	11.15
T_{xx}(MHz)	-10.92	-10.57	-10.30
T_{yy}	-9.82	-9.48	-9.19
T_{zz}	20.74	20.06	19.49
T_{xx1}	-10.92	-10.57	-10.30
T_{yy1}	-9.82	-9.48	-9.19
T_{zz1}	20.74	20.06	19.49
Q_{xx}(a.u.)	-0.36	-0.34	-0.33
Q_{yy}	-0.06	-0.05	-0.04
Q_{zz}	0.43	0.40	0.37
Q_{xx1}	-0.36	-0.34	-0.33
Q_{yy1}	-0.06	-0.05	-0.04
Q_{zz1}	0.43	0.40	0.37

Table 4.5: Nitrogen parameter table obtained from Gaussian03 (PBE0/6-31G*/PCM) with different phenyl ring dihedral angles (degree, D)

continued table

$A_{\cdot pa}\alpha$ (rad)	1.57	0.28	0.28
$A_{\cdot pa}\beta$	0.00	0.00	0.00
$A_{\cdot pa}\gamma$	0.00	1.29	1.29
$A_{\cdot pa1}\alpha$	-1.57	-0.28	-0.28
$A_{\cdot pa1}\beta$	0.00	0.00	0.00
$A_{\cdot pa1}\gamma$	0.00	-1.29	-1.29
$Q_{\cdot pa}\alpha$(rad)	0.00	1.25	0.00
$Q_{\cdot pa}\beta$	0.00	0.03	0.00
$Q_{\cdot pa}\gamma$	0.00	-0.98	0.00
$Q_{\cdot pa1}\alpha$	0.00	-1.25	0.00
$Q_{\cdot pa1}\beta$	0.00	0.03	0.00
$Q_{\cdot pa1}\gamma$	0.00	0.98	0.00

Table 4.5: Nitrogen parameter table obtained from Gaussian03 (PBE0/6-31G*/PCM) with different phenyl ring dihedral angles (degree, D)

	EPR-III	N07D
Dihedral angle	40	45
Az	33.1	32.5
Ay	-1.20	1.70
Ax	-2.12	0.63
Aiso	9.91	11.60
$A._{pa}\alpha$ (rad)	0.28	0.28
$A._{pa}\beta$	0	0
$A._{pa}\gamma$	1.29	1.29
Q_{xx}(MHz)	-0.86	-0.84
Q_{yy}	-0.05	-0.12
Q_{zz}	0.94	0.94
$Q._{pa}\alpha$(rad)	1.25	1.25
$Q._{pa}\beta$	0.03	-0.03

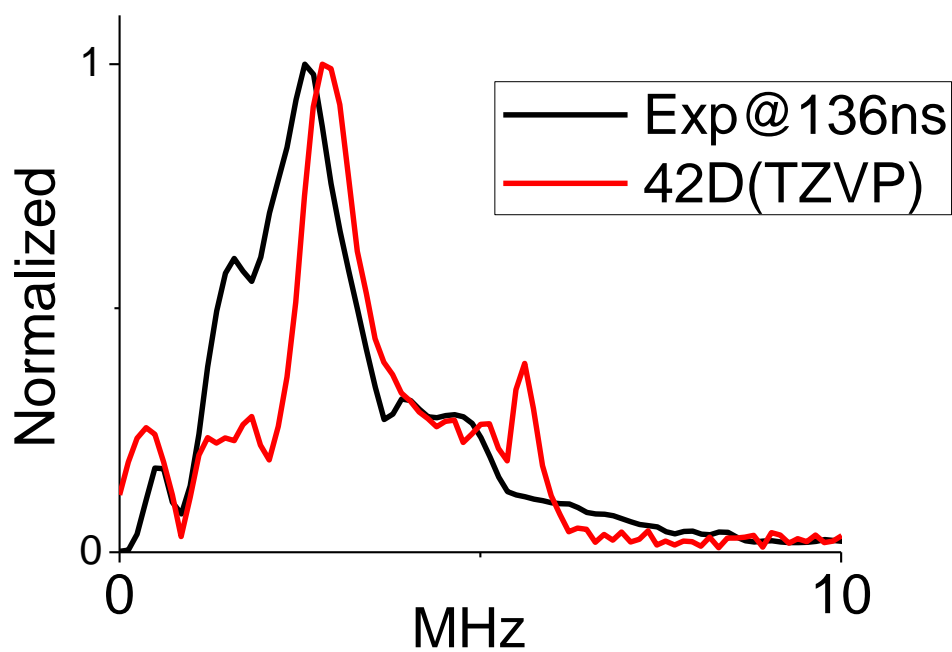Table 4.6: ^{14}N ESEEM results, BNN radical #1

(a)
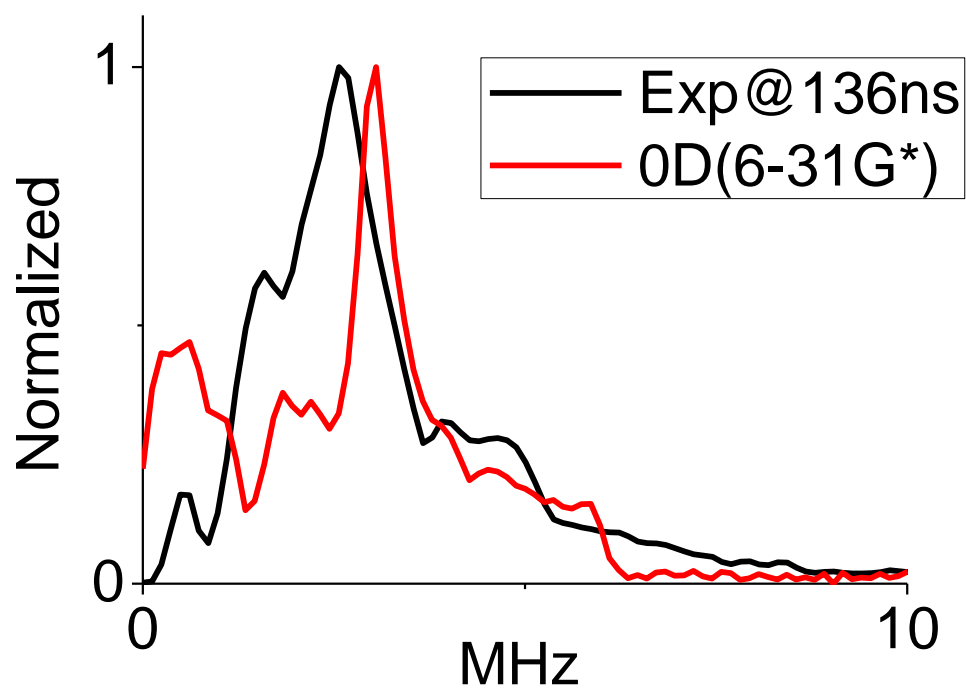
(b)
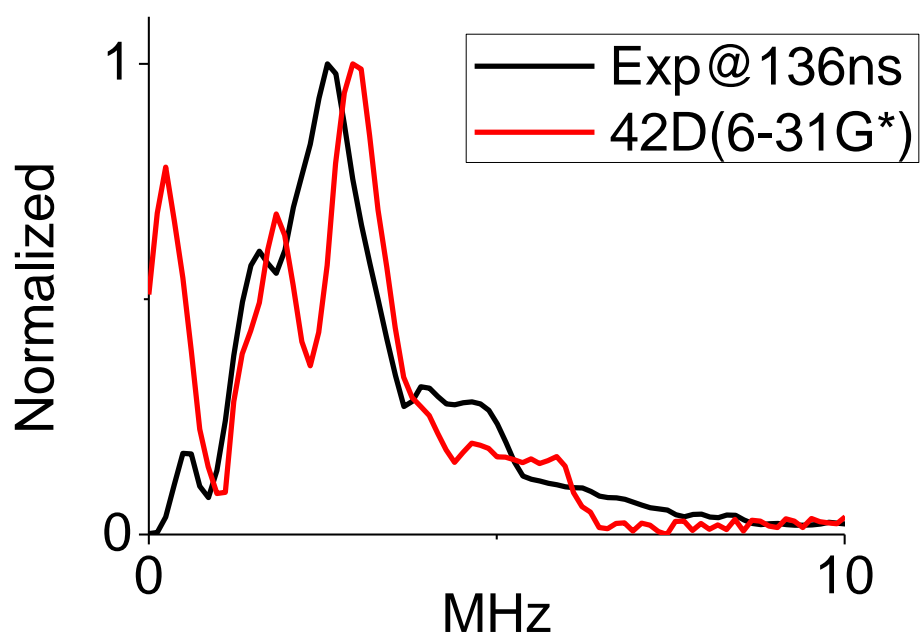
Figure 4.12 (a-c): Easyspin simulations by the parameters obtained from
PBE0/6-31G*/PCM calculation of different phenyl dihedral angles on BNN radical #1

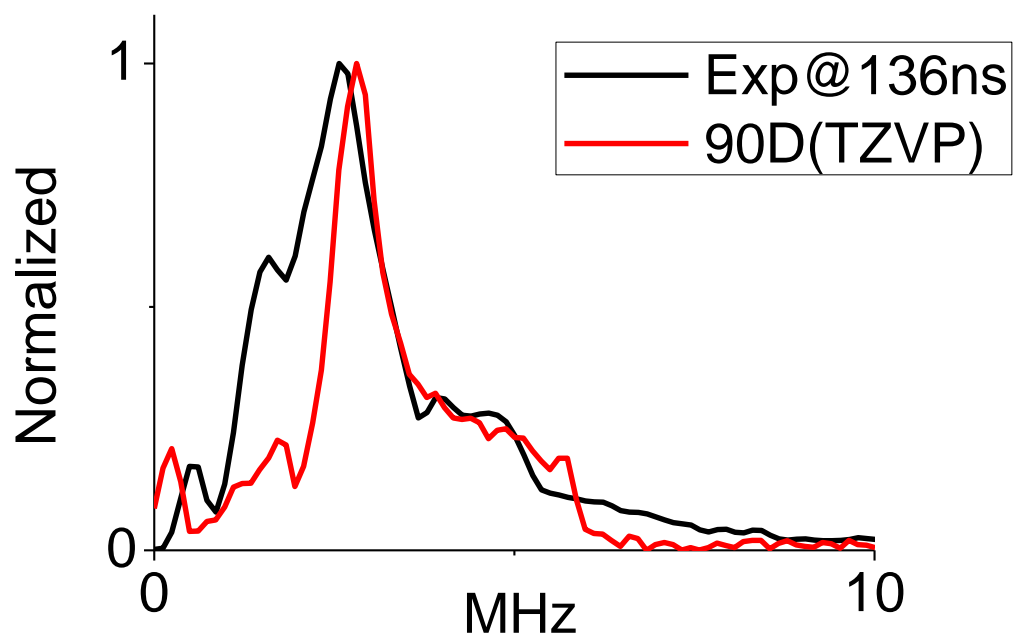and ESEEM spectrum obtained from Bruker E680 at 10 K

continued figure

(c)
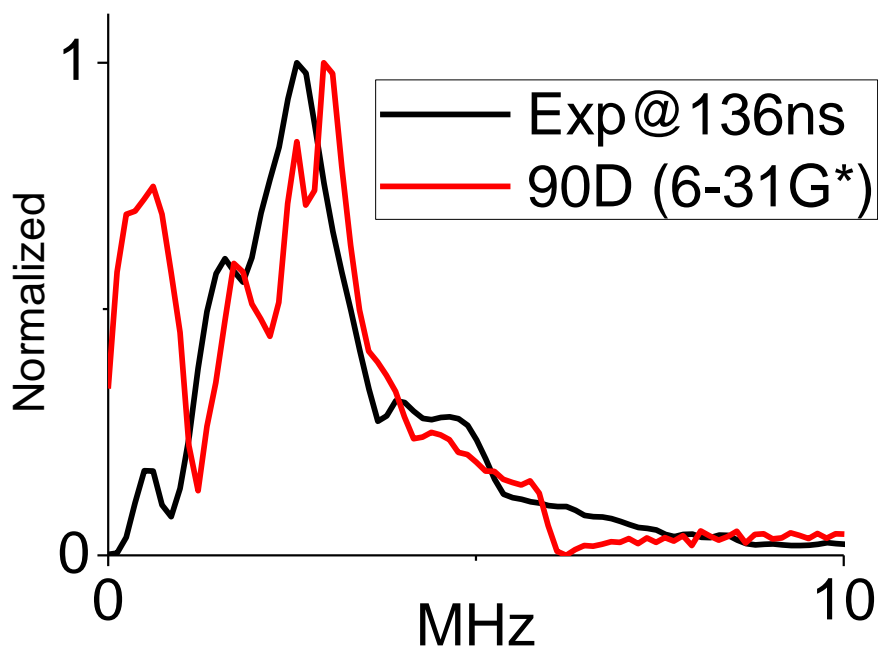
Figure 4.12 (a-c): Easyspin simulations by the parameters obtained from PBE0/6-31G* /PCM calculation of different phenyl dihedral angles on BNN radical #1 and ESEEM spectrum obtained from Bruker E680 at 10 K

Conclusion:

While the EPR-III and N07D basis sets both predict satisfactory

^{14}N-ESEEM results, the N07D basis set gives a more precise value for the

^{14}N isotropic hyperfine coupling when compared to our experimental result of

11.2 MHz. Therefore, we adopted this basis set for the analysis of BNN radical

#2.

PBE0/N07D/PCM computational model provides remarkably accurate

magnetic properties at reasonable computational costs. The parameters

calculated by PBE0/N07D/PCM fit well with ESEEM peak frequencies. We

choose PBE0/N07D/PCM method for analysis of the BNN radical #2 ESEEM

and for the analysis of the W-band ^{1}H-ENDOR spectra presented below.

Gaussian03 calculations were performed using the optimized geometry

for BNN radical #2 using the PBE0/N07D/PCM and the molecular axis system

depicted in figure 4.13. The best basis set, N07D, used with the PBE0

functional was adopted. Solvent effects were modeled with PCM. Following

the above protocol for BNN radical #1, we calculated the hyperfine coupling

principal values, the Euler angles describing the orientation of the hyperfine

coupling principal axis relative to the molecular axis system, the nuclear

quadrupole coupling principal values, and the Euler angles of nuclear

quadrupole principal axis relative to molecular axis system. In contrast to our

work on BNN radical #1, we found that the dihedral angles of the pyridyl ring

are most important for this radical because the most intense in the ESEEM

spectrum at 3.2 MHz and a shoulder at 5.6 MHz are from the pyridyl nitrogen

(figure 4.13). Our calculations show that the hyperfine coupling due to the

pyridyl nitrogen are very sensitive to the pyridyl dihedral angle. This makes the

simulation of the BNN radical #2 ESEEM spectrum dependent on the pyridyl

dihedral angle. A 9 GHz ESEEM spectrum of BNN radical #2 is shown in figure

4.13. When compared to the corresponding data from BNN radical #1, two new features are observed, a dominant peak at 3.2 MHz and a broad feature with maximum peak intensity at 5.6 MHz. The shoulder at 1.5 MHz and peak near 2.5 MHz were observed previously for BNN radical #1 and are assigned to the NO nitrogens. From the analysis of the BNN radical #1, the 0.5 MHz peak is also assigned to the NO nitrogens.
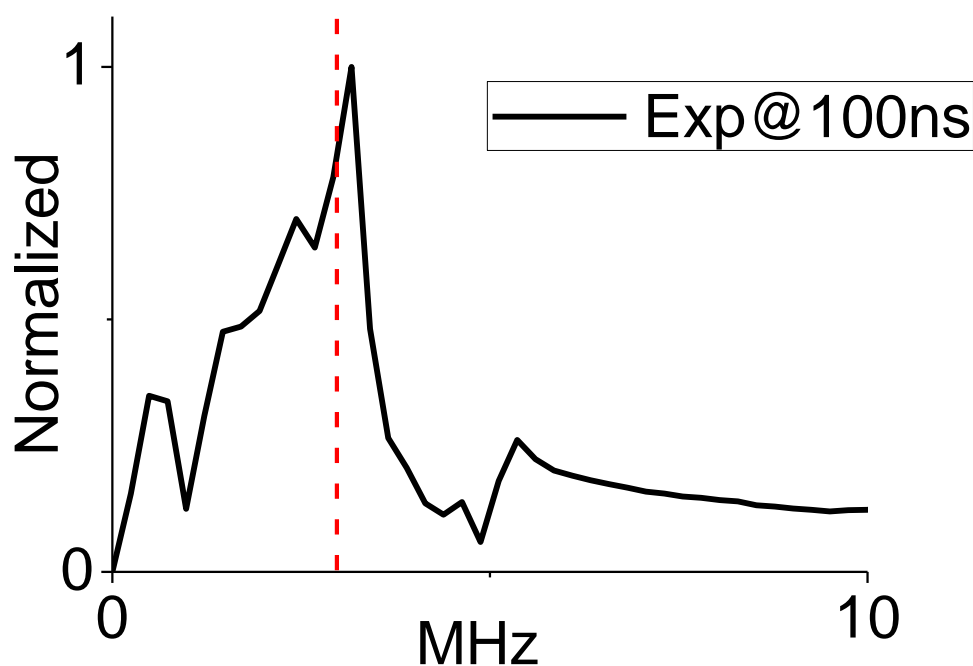
Figure 4.13: This is a frequency domain ESEEM data of the BNN radical # 2. Spectrometer conditions: magnetic field strength: 3465 G; microwave frequency : 9.729 GHz; microwave pulse power : 25 dBm; sample temperature : 10.0 K; τ value : 100 ns; T value : 40 ns. We use 100 ns due to better resolutions of 5.6 MHz peak.
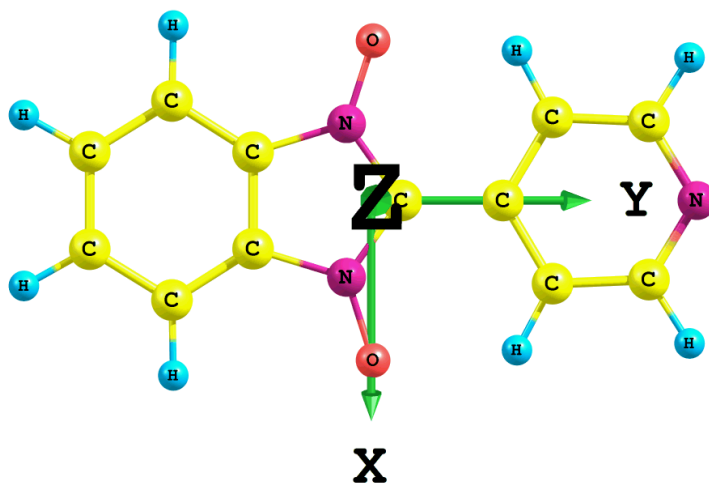
Figure 4.14: Different dihedral angles of the pyridyl ring of BNN radical #2 are calculated in Gaussian03 by PBE0/N07D/PCM.

Table 4.7 shows the results of DFT calcualtions for BNN radical #2 using the PBE0 functional with N07D basis set and PCM approximation for solvent interactions. Hyperfine and nuclear quadrupole interaction parameters are listed for all three nitrogens of the radical. The predictions of the pyridyl nitrogen are given in green and it can be readily seen that the isotropic hyperfine coupling for the pyridyl nitrogen is most dependent on the dihedral angle describing the orientation of the group's molecular plane relative to the BNN. At zero degrees, an A_{iso} value of -1.58 MHz is predicted and this value goes to zero as one varies the dihedral angle to 90°. The value of $|A_{iso}| = 1.58$ MHz is close to twice the ^{14}N Larmor frequency at our experimental magnetic field strength of 346.5 mT. Such a coupling would give rise to intense ESEEM

as shown by the work of Mims[54] and Singel[55].

The ESEEM simulations that arise from the parameters provided in table 4.7 are shown in figure 4.15. The best simulation in terms of accounting for the observed hyperfine frequencies and relative peak amplitude is spectrum 7c , where the dihedral angle describing the relative orientation of the pyridyl ring is 47 degrees. The magnetic parameters for the three nitrogens that contribute to the ESEEM spectrum are given below.

	NO nitrogens	Pyridyl N
A_z (MHz)	31.5	-0.09
A_y	1.41	-0.14
A_x	0.31	-2.26
Q_z (MHz)	0.91	2.38
Q_y	-0.10	-0.79
Q_x	-0.82	-1.58

The hyperfine couplings for the NO nitrogens are very close to the values obtained from the DFT analysis of BNN radical #1. The Euler angles describing the orientations of the hyperfine axes relative to the molecular axis system show that the principle interactions, A_z, is still along the $2p_\pi$ orbital of two nitrogen while the x and y axes are coincident with the molecular y and x

axes, respectively. Because the hyperfine tensor is nearly axial, the significance of the orientation of the A_x and A_y axes with respect to the molecular frame as provided by DFT is probably low. The hyperfine parameters for the pyridyl ^{14}N show an axial tensor with scalar and dipolar constants of 0.83 and 0.70 MHz, respectively. The Euler angles indicate that the largest coupling, -2.26 MHz, is perpendicular to the pyridyl ring while one of the two minor componetns that are close to 0 MHz lies in the direction of the electron lone pair.

The quadrupole coupling parameters for the pyridyl nitrogen yield e^2qQ = 4.754 MHz and η = 0.333, These are similar to those found in NQR studies of condensed pyridyl of e^2qQ = 4.584 MHz and η = 0.396[56].

In summary, of the ESEEM simultions shown in figure 4.15, the one using parameters derived from the 47° dihedral angle structure works best. This prediction best accounts for the frequencies of the peaks due to the NO and pyridyl nitrogens and is lacking only in the predicted relative amplitude of the NO peaks, at 1.5 and 2.5 MHz, and the dominant pyridyl peaks at 3.2 and 5.6 MHz. Figure 4.15a shows the predicted ESEEM spectrum if 10 orientations of the pyridyl ring, from 0° to 90°, are included in the calculations. While aspects of the simulation agree with the experimental data, it fails to predict the feature

at 5.6 MHz.

N07D	00D	47D	90D
a_{iso}(MHz)	11.23	11.07	10.99
$a_{iso}1$	11.23	11.07	10.99
$a_{iso}2$	-1.58	-0.83	-0.05
T_{XX}(MHz)	-11.03	-10.76	-10.66
T_{yy}	-9.92	-9.66	-9.56
T_{zz}	20.95	20.42	20.22
$T_{XX}1$	-11.03	-10.76	-10.66
$T_{yy}1$	-9.92	-9.66	-9.56
$T_{zz}1$	20.95	20.42	20.22
$T_{XX}2$	-2.69	-1.43	-0.11
$T_{yy}2$	1.33	0.69	0.02
$T_{zz}2$	1.36	0.74	0.09

Table 4.7: Nitrogen parameter table obtained from Gaussian03 (PBE0/N07D/PCM) with different pyridyl ring dihedral angles (degree, D). The green fonts are the nitrogen of the pyridyl.

continued table

Q_{xx}(a.u.)	-0.36	-0.34	-0.33
Q_{yy}	-0.04	-0.04	-0.03
Q_{zz}	0.40	0.38	0.36
$Q_{xx}1$	-0.36	-0.34	-0.33
$Q_{yy}1$	-0.04	-0.04	-0.03
$Q_{zz}1$	0.40	0.38	0.36
$Q_{xx}2$	-0.66	-0.66	-0.67
$Q_{yy}2$	-0.33	-0.33	-0.32
$Q_{zz}2$	0.99	0.99	1.00
$A._{pa}\alpha$ (rad)	1.25	1.25	1.25
$A._{pa}\beta$	0.00	0.00	0.00
$A._{pa}\gamma$	0.32	0.32	0.32
$A._{pa}1\alpha$	-1.25	-1.25	-1.25
$A._{pa}1\beta$	0.00	0.00	0.00
$A._{pa}1\gamma$	-0.32	-0.32	-0.32

Table 4.7: Nitrogen parameter table obtained from Gaussian03 (PBE0/N07D/PCM) with different pyridyl ring dihedral angles (degree, D). The green fonts are the nitrogen of the pyridyl.

continued table

A.pa2α	0.00	0.79	1.57
A.pa2β	1.57	1.57	1.57
A.pa2γ	-1.57	-1.57	-1.57
Q.paα(rad)	0.00	-1.11	0.00
Q.paβ	0.00	0.02	0.00
Q.paγ	0.00	0.79	0.00
Q.pa1α	0.00	1.11	0.00
Q.pa1β	0.00	0.02	0.00
Q.pa1γ	0.00	-0.79	0.00
Q.pa2α	0.00	0.83	1.57
Q.pa2β	1.57	1.57	1.57
Q.pa2γ	-1.57	-1.57	-1.57

Table 4.7: Nitrogen parameter table obtained from Gaussian03 (PBE0/N07D/PCM) with different pyridyl ring dihedral angles (degree, D). The green fonts are the nitrogen of the pyridyl.

(a)
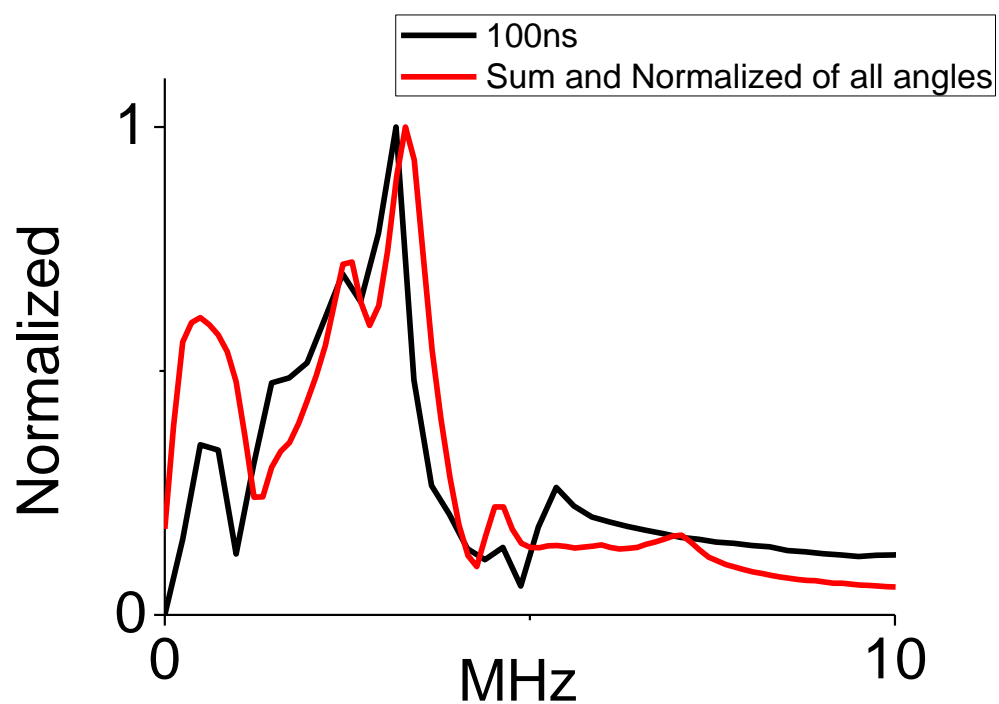
(b)
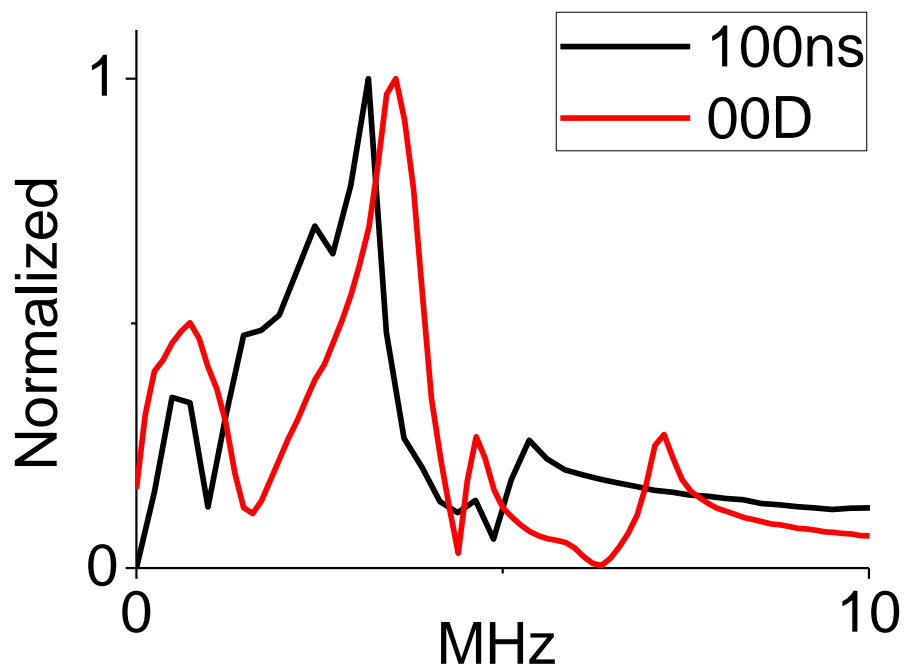
Figure 4.15 (a-d): Easyspin simulations by the parameters obtained from PBE0/N07D /PCM calculation of different pyridyl dihedral angles on BNN radical #2 and ESEEM spectrum obtained from Bruker E680 at 10 K

figure continued

(c)

(d)

Figure 4.15 (a-d): Easyspin simulations by the parameters obtained from PBE0/N07D /PCM calculation of different pyridyl dihedral angles on BNN radical #2 and ESEEM spectrum obtained from Bruker E680 at 10 K

W-band ENDOR spectroscopy

To further characterize the electronic structure of these two radicals and gain additional evidence for the dominance of the "47 degree" conformation predicted by [14]N 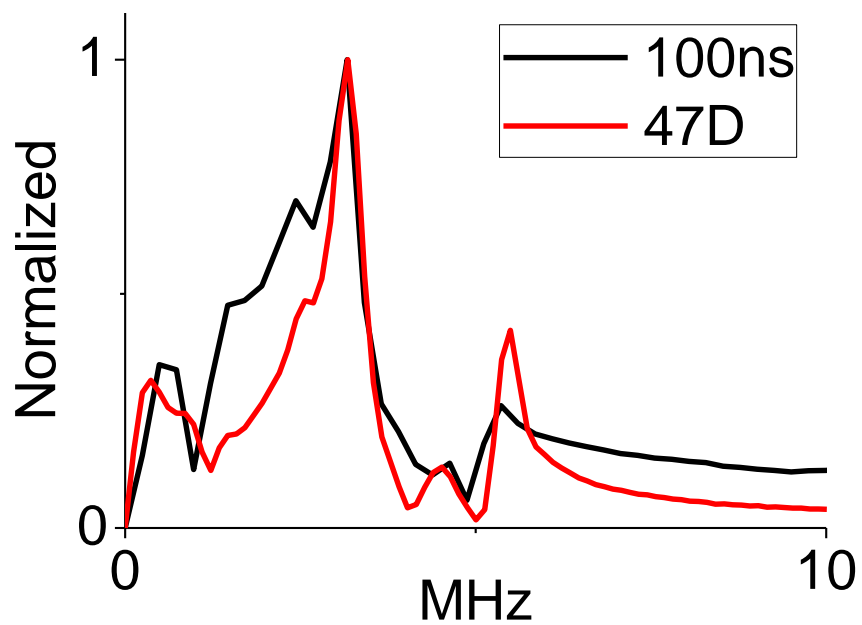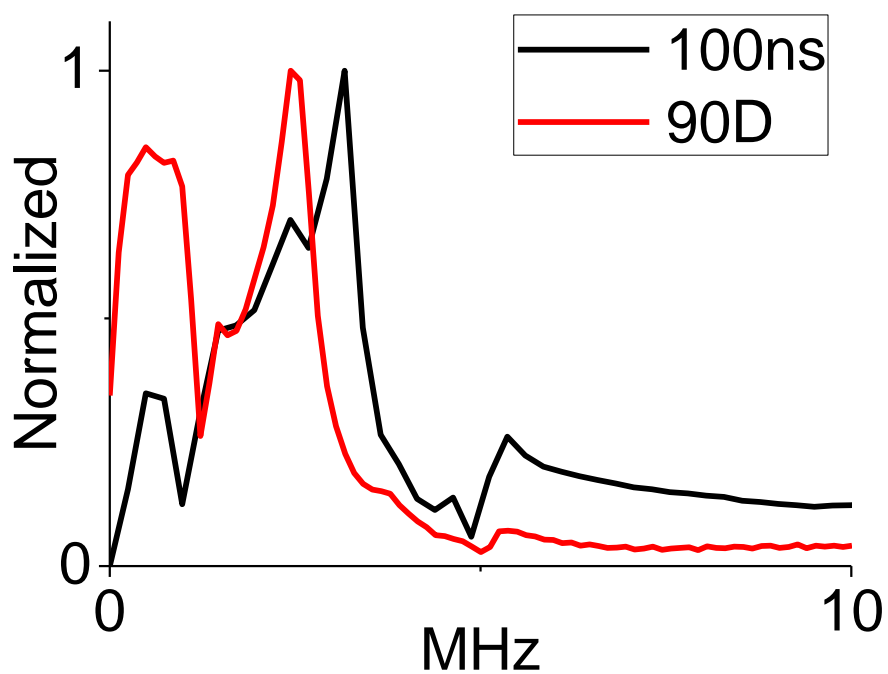ESEEM/DFT analysis, we measured their [1]H-ENDOR spectra in frozen solutions. These experiments were done at 94 GHz, where the anisotropy in the g tensor provides orientation dependent coupling to be measured. Briefly, an ENDOR experiment is done at a fixed magnetic field strength, and therefore, a fixed effective g-value, g_{eff}. This g_{eff} is given by

$$g_{eff} = \frac{\beta B}{h\nu} = \{(g_{xx}^2 \sin^2\theta \cos^2\phi + g_{yy}^2 \sin^2\theta \sin^2\phi + g_{zz}^2 \cos^2\theta)\}^{\frac{1}{2}}$$

where g_{xx}, g_{yy}, and g_{zz} are the principal values of the g tensor and θ, ϕ describe the orientation of the magnetic field, B, with respect to the g tensor axes. Thus, at a fixed field, only θ, ϕ combinations that satisfy the above equation contribute to the data. The effect of this "orientation selection" on [1]H-ENDOR spectra was illustrated by Hurst[57], et al.

The black traces of figures 4.16 and 4.18 show W-band ^{1}H ENDOR spectra collected for BNN radical #1 near the g_x (figure 4.18a), g_y (figure 4.16a), and g_z (figure 4.18b) orientations of the g tensor at 3342.3, 3351.3, and 3358.2 mT, respectively. These data were collected with identical ENDOR pulse sequences and show pronounced lineshape difference arising from

orientation selection. The spectra are centered at the proton Larmor frequency

of ^{1}H, which varies from 142.3 MHz at 3342.3 mT to 143.0 MHz at 3358.2 mT.

To gain an understanding of these spectra in terms of hyperfine couplings and

their relationship to molecular structure, we turned to DFT calculations. Figure

4.17 (top) provides a numbering scheme for the protons of BNN radical #1.

Table 4.6 shows the results of DFT calculations with respect to these nuclei.

The table is presented as above, with the columns providing coupling

constants and Euler angles obtained for four different values of the phenyl

group dihedral angle, 0°, 43°, 47°, and 90°. These results show that the ^{1}H

hyperfine couplings most sensitive to the orientations of the phenyl group are

those from H-16 and H-18. These couplings are influenced by a strong

dipole-dipole interaction with the unpaired spin density concentrated on the

NO group. This dipolar field shows T = 3.45 MHz at 0° dihedral angle and only

0.75 MHz at 90° because of the change in distances and electronic structure

that occur as the molecule goes from its planar to perpendicular orientations.

For the 0°, 43° and 47° angles, the strongest hyperfine coupling due to H16

and H18 would be resolved along g_y, at 3351.3 mT. The simulations in figure

4.16 (red traces) show this feature as a pair of peaks that are separated by

nearly 11 MHz at 0° dihedral angle (figure 4.16a) and drop to just over 3 MHz

at 90° (figure 4.16d). The data at 43° and 47° show the extremes of this coupling at 140.0 and 145.5 MHz, matching the experimental data. The traces shown in red in figure 4.16 are simulations for all of the proton couplings listed in table 4.6. It is clear that an intermediate dihedral angle of 45° best accounts for these data. A composite drawing showing how all of the proton hyperfine couplings combine to yield the simulation shown in figure 4.16c (red trace) is provided in figure 4.17 (bottom).

Using the calculation results for the 47° phenyl group orientation from table 4.7, we also ran simulations of the ENDOR spectra obtained at 3342.3 mT (g_x) and 3358.2 mT (g_z), and these results are shown plotted with experimental data in figure 4.18a and 4.18b, respectively.

(a)
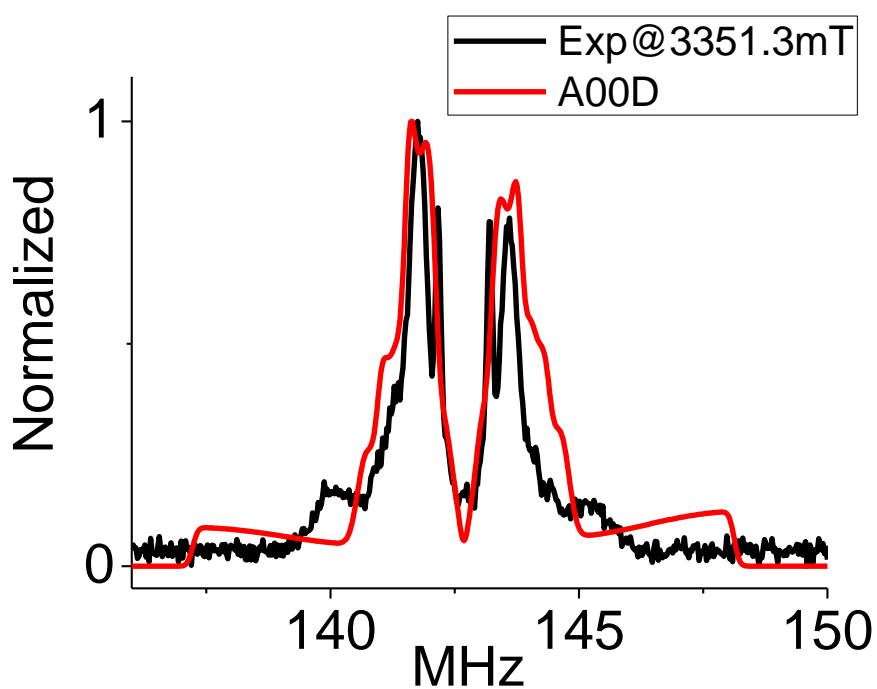
(b)
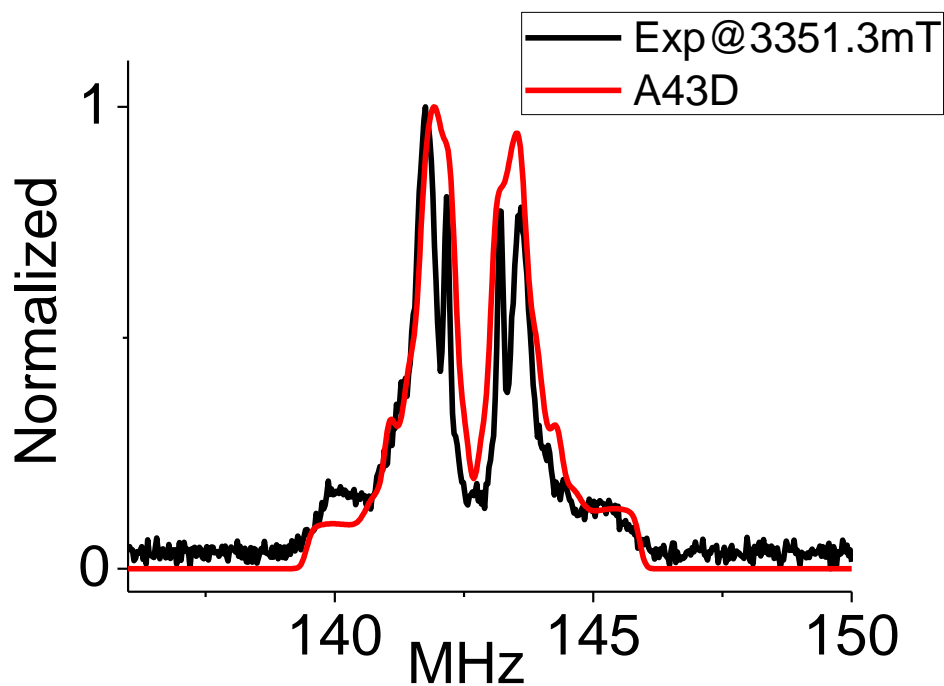
Figure 4.16 (a-d): Easyspin simulation by PBE0/N07D/PCM parameters and BNN radical #1 ENDOR spectrum at magnetic field = 3351.3 mT

continued figure
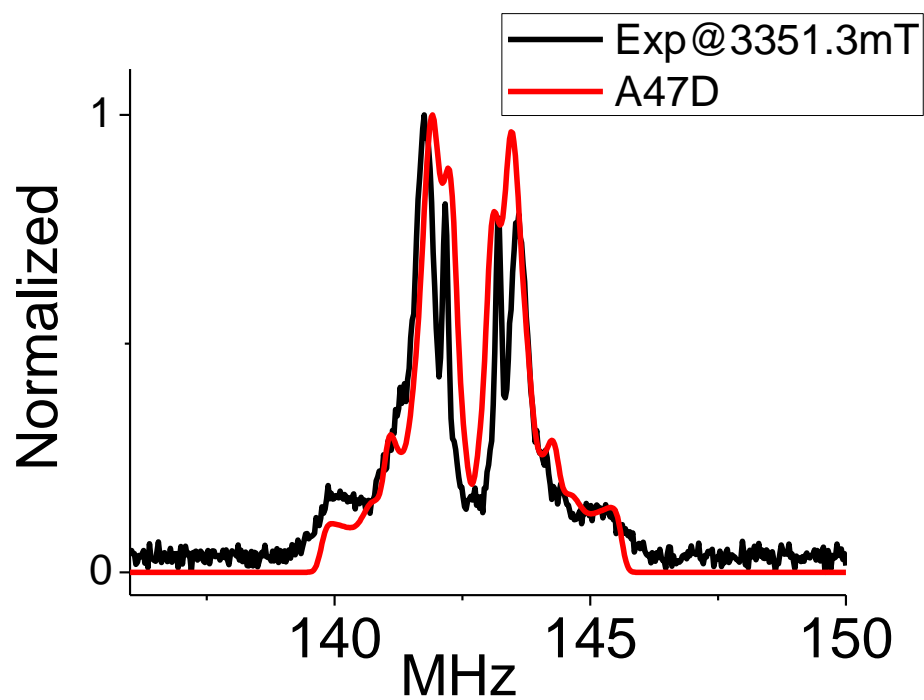
(c)

Figure 4.16 (a-d): Easyspin simulation by PBE0/N07D/PCM parameters and BNN radical #1 ENDOR spectrum at magnetic field = 3351.3 mT

figure continued

(d)
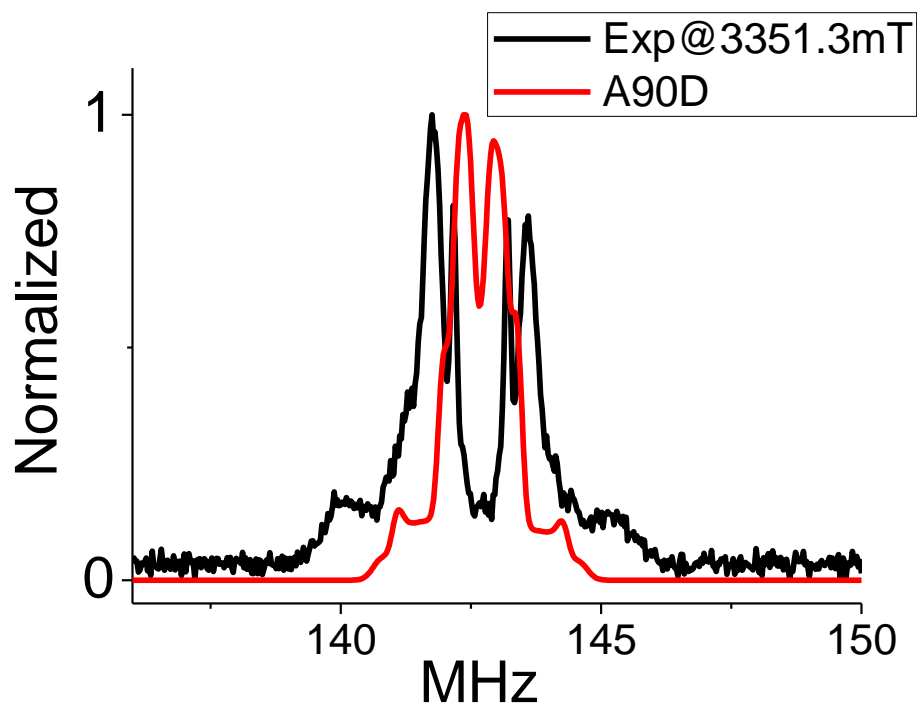
Figure 4.16 (a-d): Easyspin simulation by PBE0/N07D/PCM parameters and BNN radical #1 ENDOR spectrum at magnetic field = 3351.3 mT
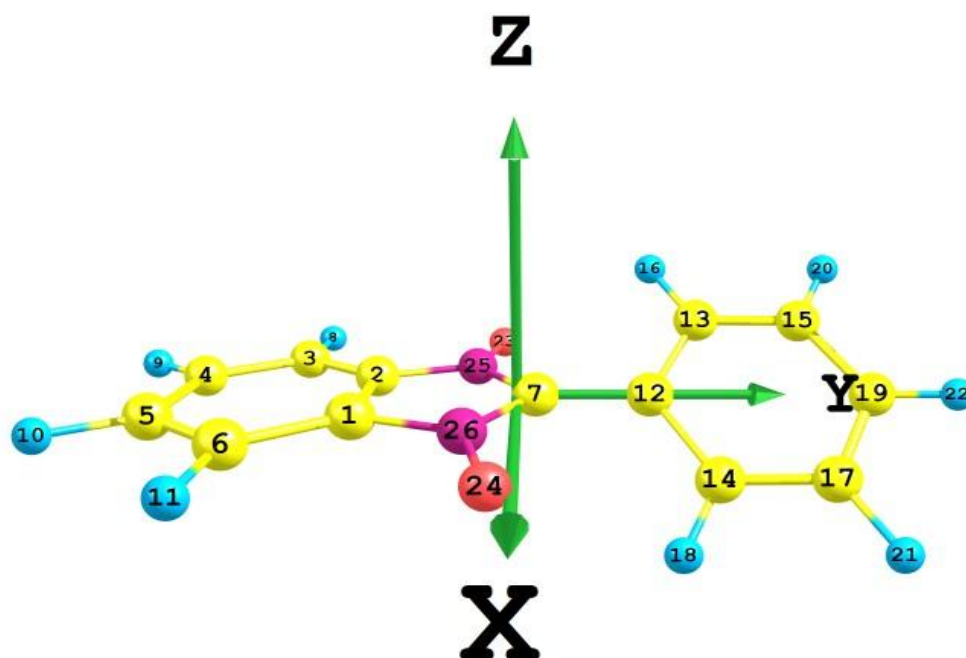
Figure 4.17: This is an Easyspin ENDOR simulation of the 47 degree phenyl dihedral angle of BNN radical #1 with PBE0/N07D/PCM parameters. We can proof that two small shoulders at 140.0 MHz and 145.5 MHz only contribute from H18 and H16 and

they are dependent of phenyl dihedral angles. ENDOR simulation is a frequency histogram so peak intensity doesn't matter.

figure continued
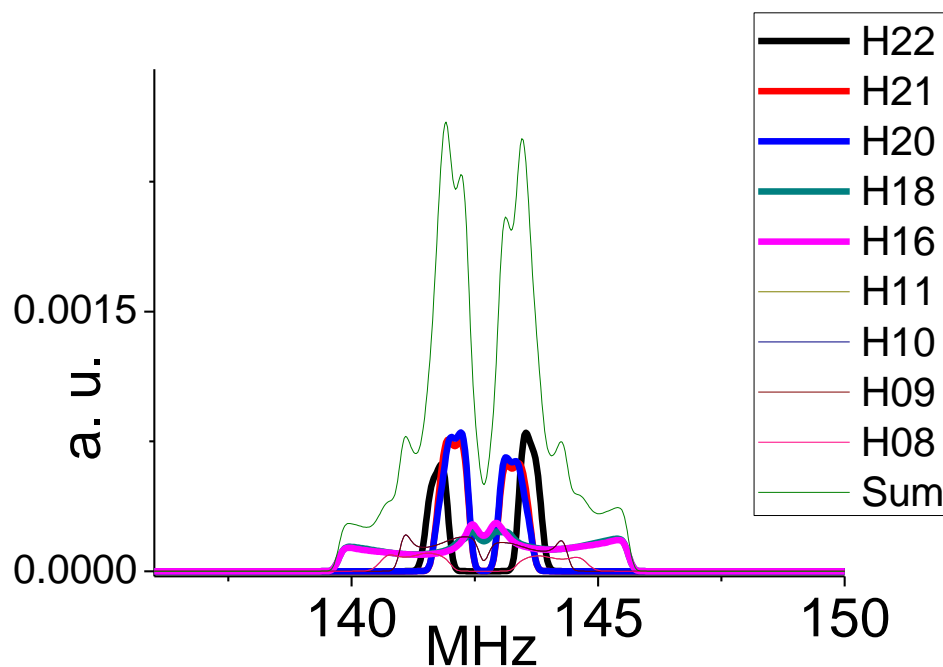
Figure 4.17: This is an Easyspin ENDOR simulation of the 47 degree phenyl dihedral angle of BNN radical #1 with PBE0/N07D/PCM parameters. We can proof that two small shoulders at 140.0 MHz and 145.5 MHz only contribute from H18 and H16 and they are dependent of phenyl dihedral angles. ENDOR simulation is a frequency histogram so peak intensity doesn't matter.

PBE0_N07D_PCM	00D	43D	47D	90D
aH8(MHz)	-3.19	-3.05	-3.04	-2.97
aH9	-2.33	-2.29	-2.29	-2.27
aH10	-2.33	-2.29	-2.29	-2.27
aH11	-3.19	-3.05	-3.04	-2.97
aH16	4.00	2.32	2.11	0.65
aH18	4.00	2.32	2.11	0.65
aH20	-1.84	-1.40	-1.32	-0.71
aH21	-1.84	-1.40	-1.32	-0.71
aH22	3.69	2.20	1.94	0.17
Txx8(MHz)	-1.92	-1.90	-1.90	-1.88
Tyy8	0.17	0.14	0.14	0.13
Tzz8	1.75	1.76	1.76	1.75
Txx9	-1.39	-1.37	-1.36	-1.35
Tyy9	-0.79	-0.77	-0.77	-0.76
Tzz9	2.17	2.13	2.13	2.11

Table 4.8: Proton parameter table obtained from Gaussian03 (PBE0/N07D/PCM) with different phenyl ring dihedral angles (degree, D)

continued table

Txx21	-0.71	-0.61	-0.59	-0.38
Tyy21	-0.14	-0.09	-0.09	-0.10
Tzz21	0.85	0.70	0.68	0.48
Txx22	-1.21	-0.55	-0.44	-0.18
Tyy22	-0.37	-0.27	-0.25	-0.14
Tzz22	1.58	0.82	0.69	0.32
A.paα8(rad)	0.00	0.00	0.00	0.00
A.paβ8	1.57	-1.57	-1.57	1.57
A.paγ8	1.01	1.05	1.05	1.01
A.paα9	1.57	1.57	1.57	1.57
A.paβ9	1.57	1.57	1.57	1.57
A.paγ9	1.27	1.27	1.27	1.27
A.paα10	1.57	1.57	1.57	1.57
A.paβ10	1.57	-1.57	-1.57	1.57
A.paγ10	-1.27	-1.27	-1.27	-1.27

Table 4.8: Proton parameter table obtained from Gaussian03 (PBE0/N07D/PCM) with different phenyl ring dihedral angles (degree, D)

continued table

A.paα11	0.00	0.00	0.00	0.00
A.paβ11	1.57	1.57	1.57	1.57
A.paγ11	-1.01	-1.05	-1.05	-1.01

Table 4.8: Proton parameter table obtained from Gaussian03 (PBE0/N07D/PCM) with different phenyl ring dihedral angles (degree, D)

continued table

|				
A.paα16	1.57	0.55	0.51	1.57
A.paβ16	1.57	-1.03	-1.01	1.57
A.paγ16	-1.43	1.44	1.39	-1.43
A.paα18	1.57	0.55	0.51	1.57
A.paβ18	1.57	1.03	1.01	1.57
A.paγ18	1.43	-1.44	-1.39	1.43
A.paα20	1.57	0.58	0.49	1.57
A.paβ20	1.57	-1.07	-1.06	1.57
A.paγ20	-0.94	-1.27	-1.33	-0.94
A.paα21	1.57	0.58	0.49	1.57
A.paβ21	1.57	1.07	1.06	1.57
A.paγ21	0.94	1.27	1.33	0.94
A.paα22	1.57	1.57	1.57	1.57
A.paβ22	1.57	0.00	0.00	1.57
A.paγ22	0.00	0.00	0.00	0.94

Table 4.8: Proton parameter table obtained from Gaussian03 (PBE0/N07D/PCM) with different phenyl ring dihedral angles (degree, D)

(a)
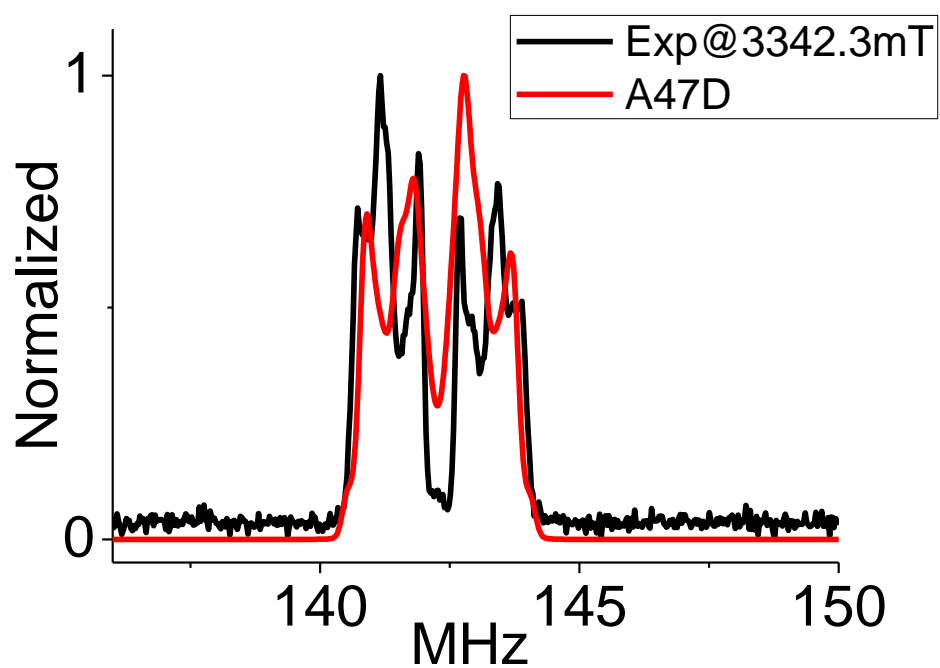
(b)
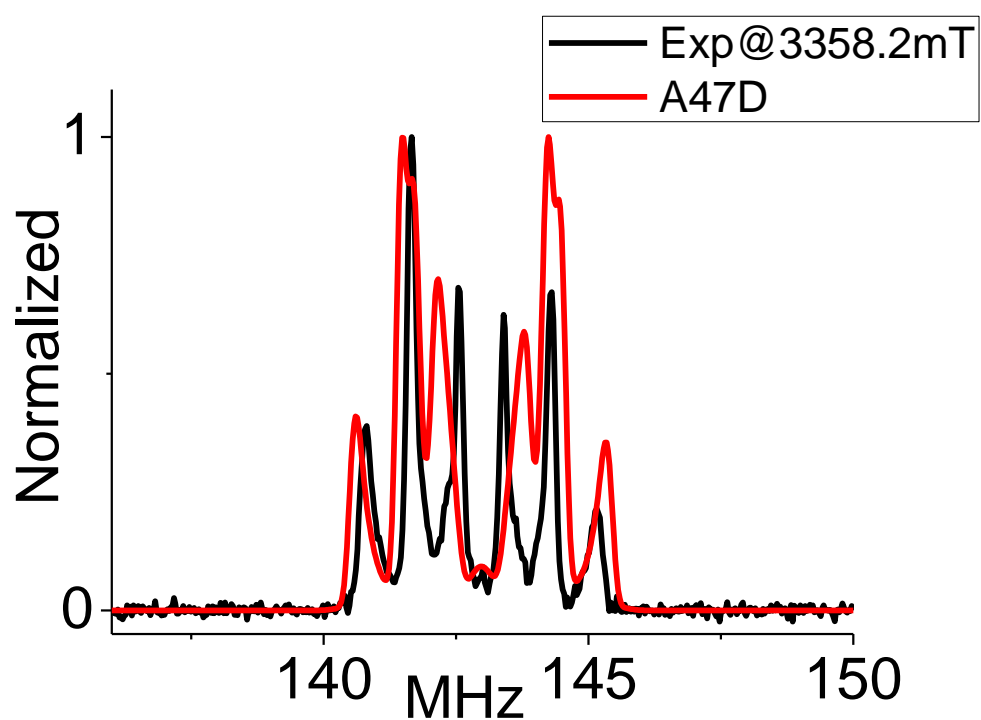
Figure 4.18 (a-b): BNN radical #1 ENDOR spectrum at magnetic fields 3342.3 mT and 3358.2 mT

The black traces in figure 4.19 and 4.21 show the ^{1}H ENDOR spectra

obtained for BNN radical #2 at magnetic field position near the principal values

of the radical's g-tensor. An analogs procedure identical to that used for BNN

radical #1 was done and numerical results are provided in table 4.8. The best

simulation as judged by the predicted frequencies, were found for a pyridyl

dihedral angle at 40° and shown in figure 4.19b (g_y component), 21a (g_z

component) and 21b (g_x component).

(a)
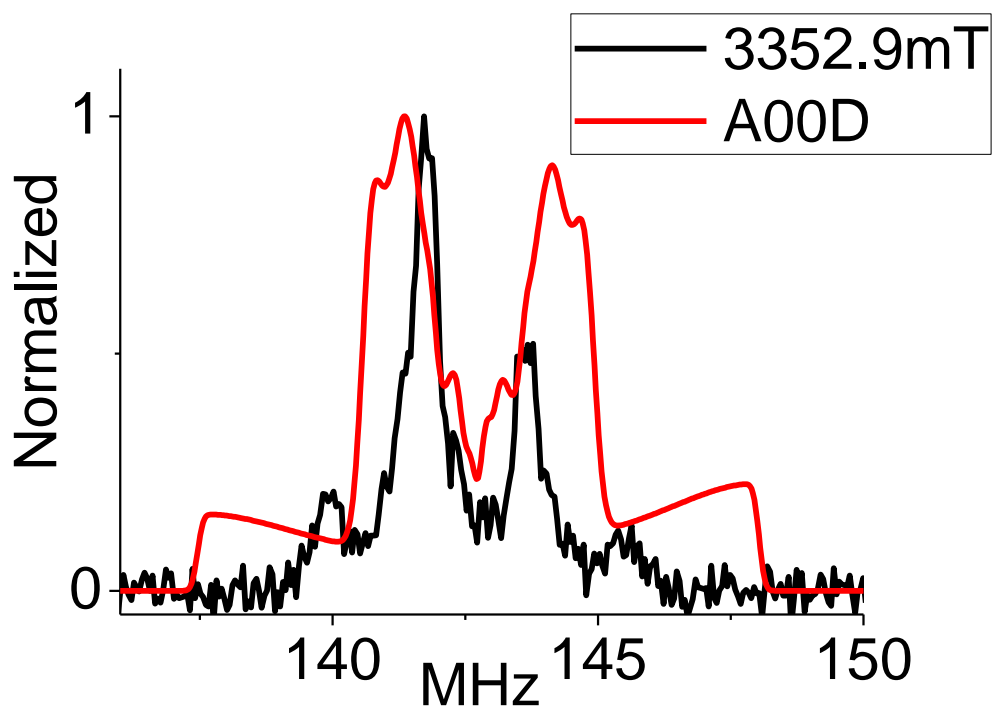
Figure 4.19 (a-c): Easyspin simulation with PBE0/N07D/PCM parameters and BNN #2
ENDOR spectra at magnetic field = 3352.9 mT

figure continued

(b)
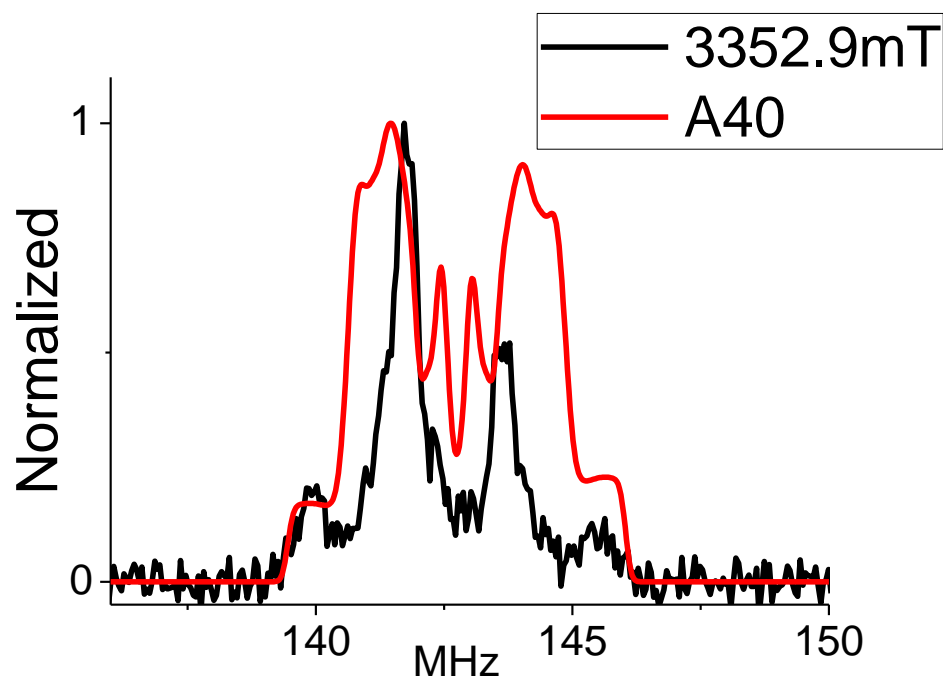
(c)
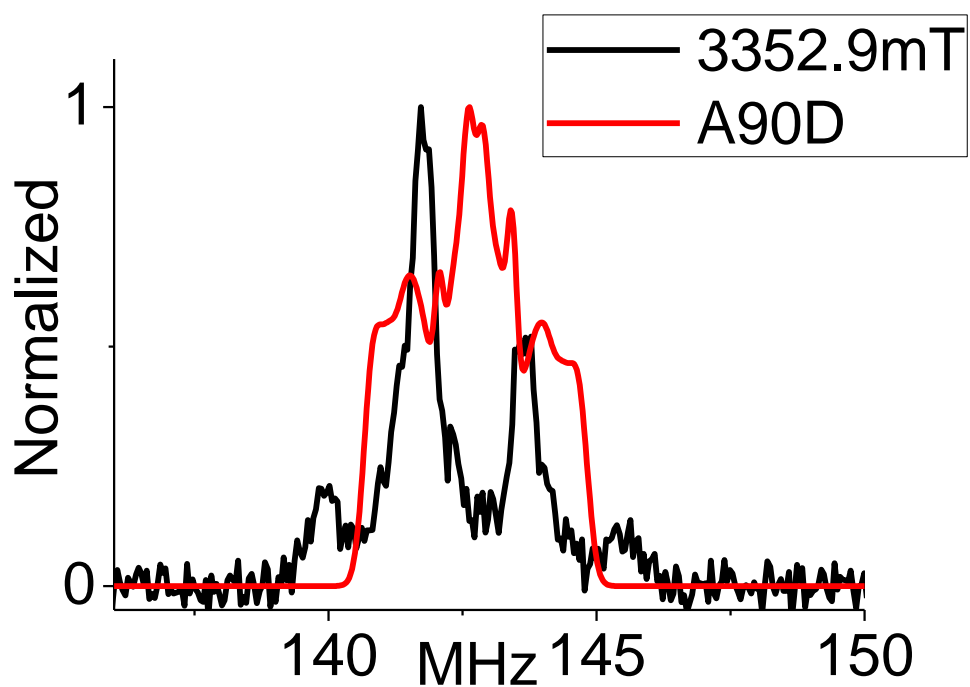
Figure 4.19 (a-c): Easyspin simulation with PBE0/N07D/PCM parameters and BNN #2
ENDOR spectra at magnetic field = 3352.9 mT
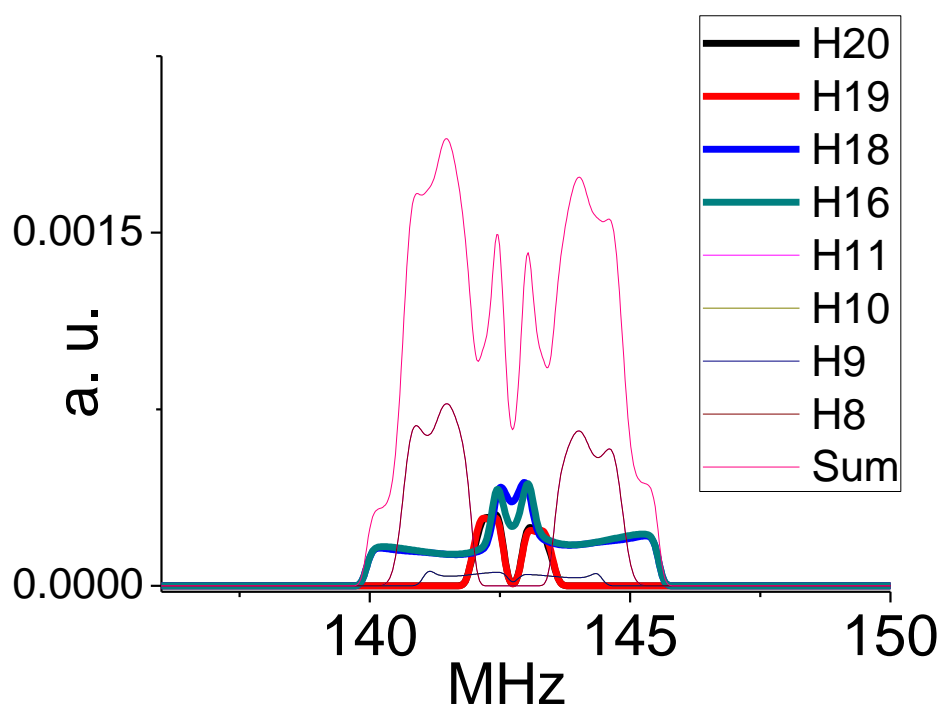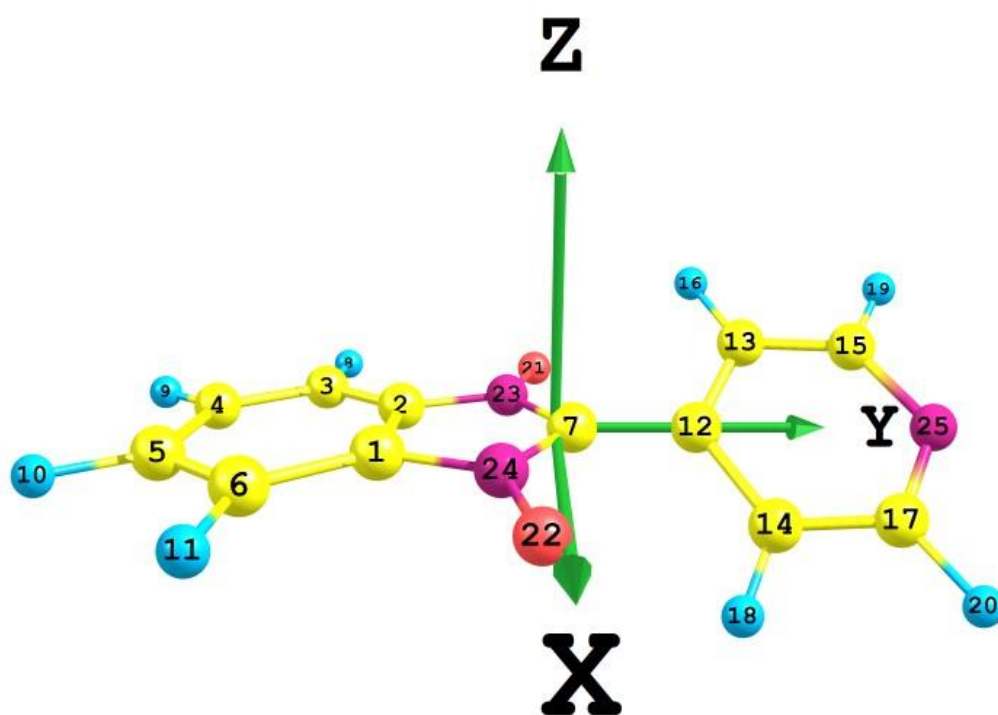
Figure 4.20: This is an Easyspin ENDOR simulation of the 47 degree pyridyl dihedral angle of BNN radical #2 with PBE0/N07D/PCM parameters. ENDOR simulation is a frequency histogram so peak intensity doesn't matter.

PBE0_N07D_PCM	0D	40D	90D
aH8(MHz)	-3.32	-3.18	-3.10
aH9	-2.33	-2.31	-2.30
aH10	-2.33	-2.31	-2.30
aH11	-3.32	-3.18	-3.10
aH16	3.59	2.18	0.58
aH18	3.59	2.18	0.58
aH19	-1.37	-1.13	-0.65
aH20	-1.37	-1.13	-0.65
Txx8(MHz)	-1.86	-1.85	-1.83
Tyy8	0.25	0.23	0.22
Tzz8	1.61	1.62	1.61
Txx9	-1.39	-1.38	-1.37

Table 4.9: Proton parameter table obtained from Gaussian03 (PBE0/N07D/PCM) with different pyridyl ring dihedral angles (degree, D)

continued table

Tyy9	-0.78	-0.77	-0.76
Tzz9	2.18	2.15	2.13
Txx10	-1.39	-1.38	-1.37
Tyy10	-0.78	-0.77	-0.76
Tzz10	2.18	2.15	2.13
Txx11	-1.86	-1.85	-1.83
Tyy11	0.25	0.23	0.22
Tzz11	1.61	1.62	1.61
Txx16	-3.94	-2.90	-1.45
Tyy16	-3.05	-1.50	0.56
Tzz16	6.99	4.41	0.89
Txx18	-3.94	-2.90	-1.45
Tyy18	-3.05	-1.50	0.55
Tzz18	6.99	4.41	0.89

Table 4.9: Proton parameter table obtained from Gaussian03 (PBE0/N07D/PCM) with different pyridyl ring dihedral angles (degree, D)

continued table

Txx19	-0.60	-0.56	-0.39
Tyy19	-0.17	-0.12	-0.12
Tzz19	0.78	0.69	0.51
Txx20	-0.60	-0.56	-0.39
Tyy20	-0.17	-0.12	-0.12
Tzz20	0.78	0.69	0.51
A.paα8(rad)	0.00	0.00	0.00
A.paβ8	1.57	1.57	1.57
A.paγ8	-0.92	-0.97	-0.99
A.paα9	1.57	1.57	1.57
A.paβ9	1.57	-1.57	1.57
A.paγ9	-1.28	-1.28	-1.28

Table 4.9: Proton parameter table obtained from Gaussian03 (PBE0/N07D/PCM) with different pyridyl ring dihedral angles (degree, D)

continued table

A.paα10	1.57	1.57	1.57
A.paβ10	-1.57	1.57	-1.57
A.paγ10	1.28	1.28	1.28
A.paα11	0.00	0.00	0.00
A.paβ11	-1.57	-1.57	-1.57
A.paγ11	0.92	0.97	0.99
A.paα16	1.57	0.53	0.00
A.paβ16	1.57	1.05	1.08
A.paγ16	1.46	-1.46	-1.57
A.paα18	1.57	0.53	-0.14
A.paβ18	1.57	-1.05	-1.08
A.paγ18	-1.46	1.46	1.57

Table 4.9: Proton parameter table obtained from Gaussian03 (PBE0/N07D/PCM) with different pyridyl ring dihedral angles (degree, D)

continued table

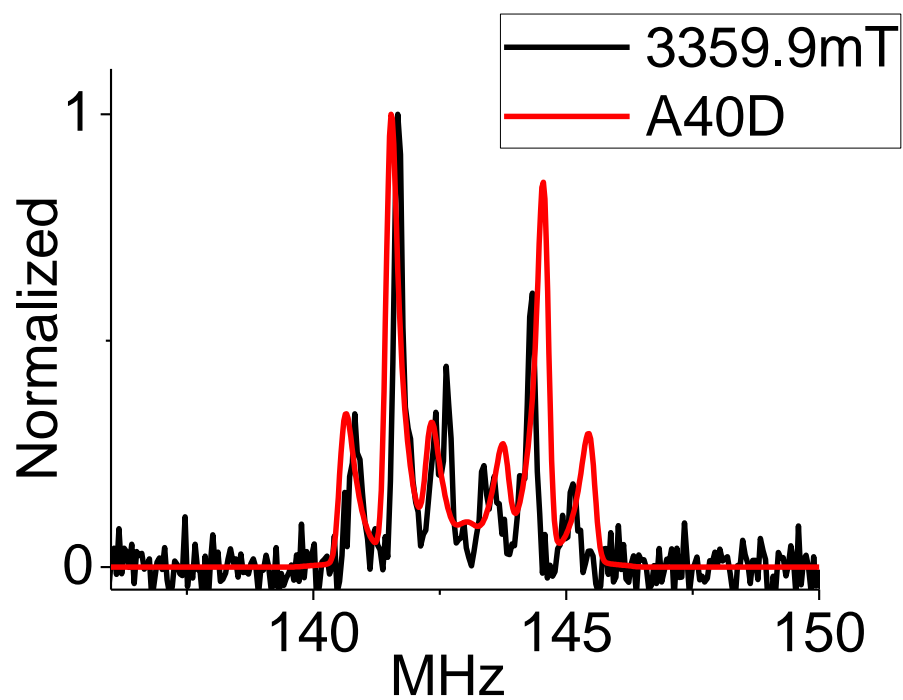|			
A.paα19	1.57	0.62	0.00
A.paβ19	1.57	1.11	1.19
A.paγ19	1.01	1.30	-1.57
A.paα20	1.57	0.62	0.00
A.paβ20	1.57	-1.11	-1.19
A.paγ20	-1.01	-1.30	-1.57

Table 4.9: Proton parameter table obtained from Gaussian03 (PBE0/N07D/PCM) with different pyridyl ring dihedral angles (degree, D)

(a)

(b)
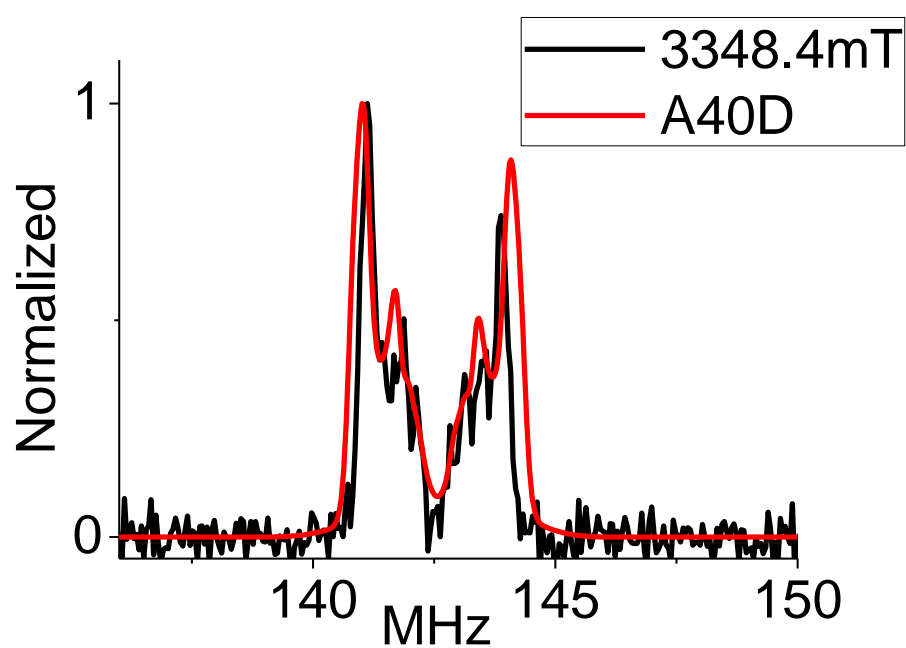
Figure 4.21 (a-b): BNN radical #2 ENDOR spectrum and Easyspin ENDOR simulation at magnetic fields 3359.9 mT (a) and 3348.4 mT (b)

Chapter 5

Potential energy surfaces (PES) of BNN radical #1 and #2

The results of our ^{14}N-ESEEM and ^{1}H-ENDOR experiments lead to the conclusion that both BNN radicals studied in this thesis prefer a conformation in frozen toluene when the plane of the phenyl or pyridyl group are at 45° angle with respect to the plane of the BNN group. To suggest these finding further, we undertook calculations of the potential energy surface. We found that UHF-reference QCISD, a quadratic configuration iteration calculation including single and double substitutions, predicted 40° dihedral angle as the minimum energy conformation for both BNN radical #1 and #2 in toluene environments. These results are shown in figure 5.1.

(a)

BNN radical #1_UHF-QCISD_6-31G*_toluene

(b)

BNN radical #2_UHF-QCISD_6-31G*_toluene
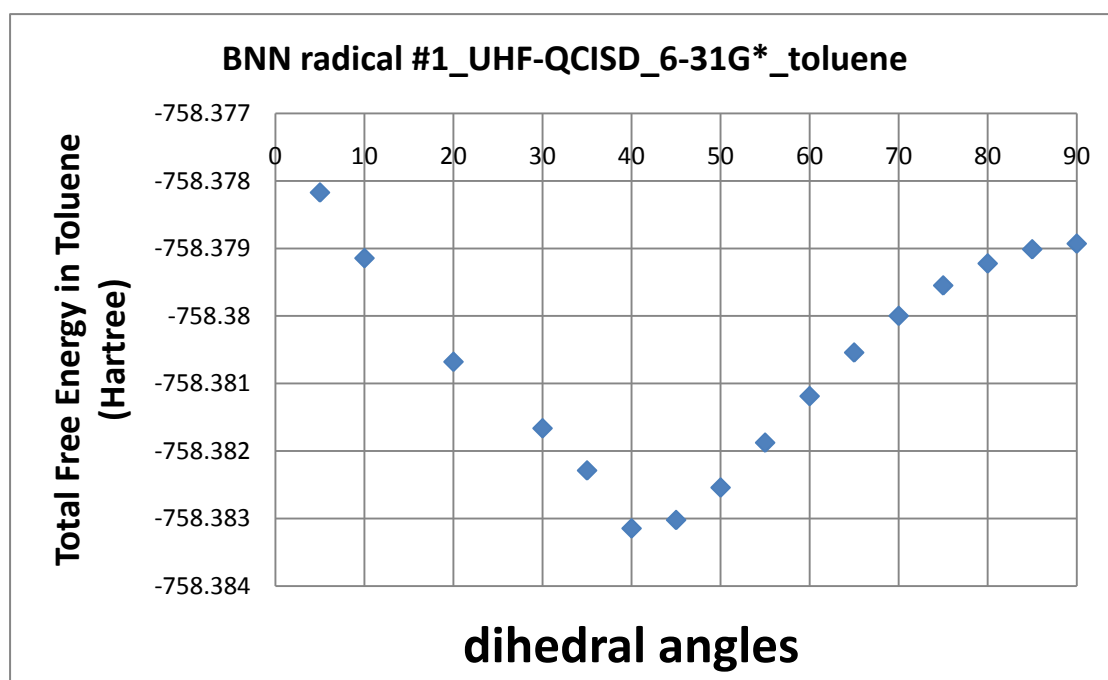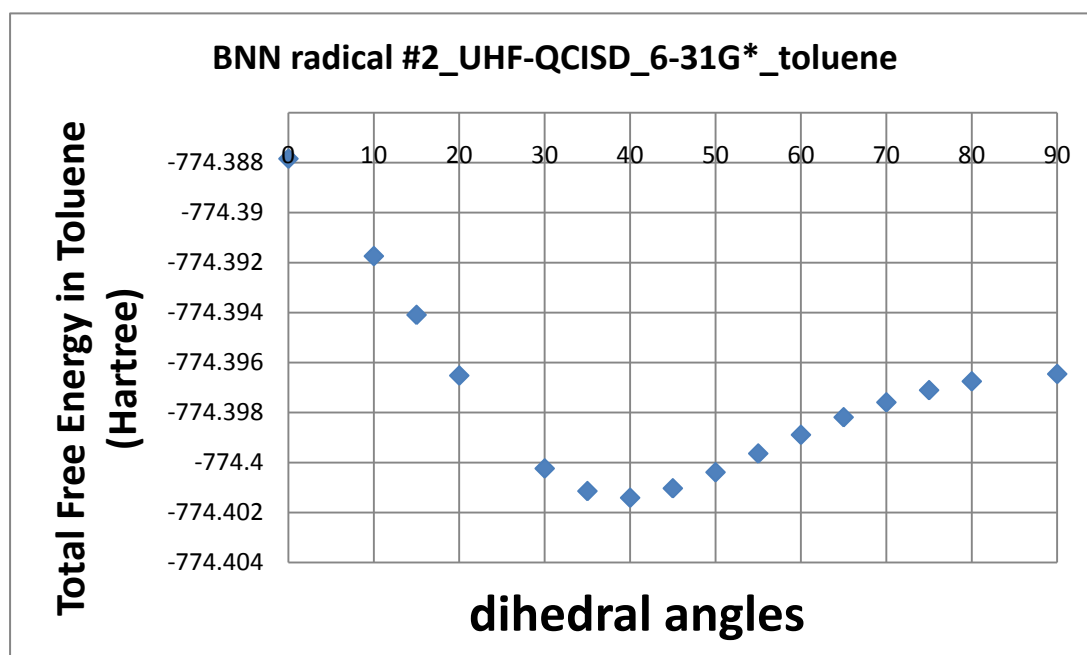
Figure 5.1 (a-b): UHF reference QCISD, a quadratic configuration iteration calculation including single and double substitutions by Pople[58] is in fair agreement with our experiment at 10 K in which the minimum energy conformation is in the pyridyl or phenyl ring near 40 degree dihedral angle.[59]

Chapter 6

Conclusion

The present article reports the results of a systematic computational and experimental study devoted to a better understanding of magneto-structural relationships in BNNs. From a methodological point of view, the results derived by Barone's PBE0/N07D/PCM model for structural and magnetic properties, which are accurate enough to allow for quantitative studies, are in excellent accord with the information derived from ESEEM and ENDOR and the potential energy surface by UHF-reference QCISD/6-31G*/PCM. We were thus able to unravel the role of different factors (both structural and electronic) in tuning the magnetic properties of nitrogen free radicals.

Bibliography

Bibliography

1.   Swartz, N.K.a.H.M., *Nitroxide Spin Labels*, New York: CRC Press.

2.   Buchaklian, A.H. and C.S. Klug, *Characterization of the walker a motif of MsbA using site-directed spin-labeling electron paramagnetic resonance spectroscopy.* Biochemistry, 2005. **44**(14): p. 5503-5509.

3.   Tedeschi, A.M., et al., *Micellar aggregation of sulfonate surfactants studied by electron paramagnetic resonance of a cationic nitroxide: an experimental and computational approach.* Physical Chemistry Chemical Physics, 2002. **4**(11): p. 2180-2188.

4.   Improta, R. and V. Barone, *Interplay of Electronic, Environmental, and Vibrational Effects in Determining the Hyperfine Coupling Constants of Organic Free Radicals.* Chemical Reviews, 2004. **104**(3): p. 1231-1254.

5.   Mattar, S.M. and A.D. Stephens, *UB1LYP hybrid density functional studies of the 2,2,6,6-tetramethyl-4-piperidone-oxyl (TEMPONE) hyperfine tensors.* Chemical Physics Letters, 2000. **319**(5-6): p. 601-610.

6.   Arbuznikov, A.V., et al., *Validation study of meta-GGA functionals and of a model exchange-correlation potential in density functional calculations of EPR parameters.* Physical Chemistry Chemical Physics, 2002. **4**(22): p. 5467-5474.

7.   Barone, V. and A. Polimeno, *Toward an integrated computational approach to CW-ESR spectra of free radicals.* Physical Chemistry Chemical Physics, 2006. **8**(40): p. 4609-4629.

8.   Mattar, S.M., *Minimum general requirements for equivalent atoms in a molecule.* Chemical Physics Letters, 1998. **287**(5-6): p. 608-612.

9.   Mattar, S.M., *Role of the Solvent in Computing the 1,4-Benzosemiquinone g-Tensor by the Coupled-Perturbed Kohn–Sham Hybrid Density Functional Method†.* The Journal of Physical Chemistry B, 2004. **108**(27): p. 9449-9455.

10. Atanasov, M., et al., *The calculation of ESR parameters by density functional theory: the g- and A-tensors of Co(acacen).* Chemical Physics Letters, 2004. **399**(4-6): p. 433-439.

11. Schöneboom, J.C., F. Neese, and W. Thiel, *Toward Identification of the Compound I Reactive Intermediate in Cytochrome P450 Chemistry: A QM/MM Study of Its EPR and Mössbauer Parameters.* Journal of the American Chemical Society, 2005. **127**(16): p. 5840-5853.

12. Astashkin, A.V., et al., *Pulsed EPR Investigations of Systems Modeling Molybdenum Enzymes: Hyperfine and Quadrupole Parameters of Oxo-17O in [Mo17O(SPh)4].* Journal of the American Chemical Society, 2005. **127**(47): p. 16713-16722.

13. Mattar, S.M., *Accurate Calculation of the Phenyl Radical's Magnetic Inequivalency, Relative Orientations of Its Spin Hamiltonian Tensors, and Its Electronic Spectrum.* The Journal of Physical Chemistry A, 2006. **111**(2): p. 251-260.

14. Cave, R.J. and E.R. Davidson, *HYLLERAAS VARIATIONAL PERTURBATION-THEORY - APPLICATION TO CORRELATION PROBLEMS IN MOLECULAR-SYSTEMS.* Journal of Chemical Physics, 1988. **88**(9): p. 5770-5778.

15. Perera, S.A., L.M. Salemi, and R.J. Bartlett, *Hyperfine coupling constants of organic radicals.* Journal of Chemical Physics, 1997. **106**(10): p. 4061-4066.

16. Al Derzi, A.R., S. Fau, and R.J. Bartlett, *Benchmark Study of Isotropic Hyperfine Coupling Constants for Hydrogen: Influence of Geometry, Correlation Method, and Basis Set.* The Journal of Physical Chemistry A, 2003. **107**(34): p. 6656-6667.

17. Neese, F., *Prediction of electron paramagnetic resonance g values using coupled perturbed Hartree--Fock and Kohn--Sham theory.* The Journal of Chemical Physics, 2001. **115**(24): p. 11080-11096.

18. Ciofini, I., C. Adamo, and V. Barone, *Complete structural and magnetic characterization of biological radicals in solution by an integrated quantum*

mechanical approach: Glycyl radical as a case study. The Journal of Chemical Physics, 2004. **121**(14): p. 6710-6718.

19.   Scuseria, G.E., *Linear Scaling Density Functional Calculations with Gaussian Orbitals.* The Journal of Physical Chemistry A, 1999. **103**(25): p. 4782-4790.

20.   Hermosilla, L., et al., *Density Functional Theory Predictions of Isotropic Hyperfine Coupling Constants.* The Journal of Physical Chemistry A, 2005. **109**(6): p. 1114-1124.

22.   Hermosilla, L., et al., *Theoretical Isotropic Hyperfine Coupling Constants of Third-Row Nuclei (29Si, 31P, and 33S).* The Journal of Physical Chemistry A, 2005. **109**(33): p. 7626-7635.

23.   Hermosilla, L., et al., *Density Functional Theory Study of 14N Isotropic Hyperfine Coupling Constants of Organic Radicals.* The Journal of Physical Chemistry A, 2006. **110**(50): p. 13600-13608.

24.   Hermosilla, L., P. Calle, and C. Sieiro, *Assignments of hyperfine splittings by DFT methods of radicals containing S-33 (I=3/2), P-31(I=1/2), and Si-29 (I=1/2) nuclei.* Phosphorus Sulfur and Silicon and the Related Elements, 2005. **180**(5-6): p. 1421-1422.

25.   Becke, A.D., *Density-functional thermochemistry. III. The role of exact exchange.* The Journal of Chemical Physics, 1993. **98**(7): p. 5648-5652.

26.   Lee, C., W. Yang, and R.G. Parr, *Development of the Colle-Salvetti correlation-energy formula into a functional of the electron density.* Physical Review B, 1988. **37**(2): p. 785.

27.   Godbout, N.S., Dennis R.; Andzelm, Jan; Wimmer, Erich, *Optimization of Gaussian-type basis sets for local spin density functional calculations Part I. Boron through neon, optimization technique and validation. .* Canadian Journal of Chemistry, 1992. **70**(2): p. 560.

28.   Rega, N., M. Cossi, and V. Barone, *Development and validation of reliable quantum mechanical approaches for the study of free radicals in solution.* The Journal of Chemical Physics, 1996. **105**(24): p. 11060-11067.

29. Barone, V., *Structure, Thermochemistry, and Magnetic Properties of Binary Copper Carbonyls by a Density-Functional Approach.* The Journal of Physical Chemistry, 1995. **99**(30): p. 11659-11666.

30. Hehre, W.J., R. Ditchfield, and J.A. Pople, *Self---Consistent Molecular Orbital Methods. XII. Further Extensions of Gaussian---Type Basis Sets for Use in Molecular Orbital Studies of Organic Molecules.* The Journal of Chemical Physics, 1972. **56**(5): p. 2257-2261.

31. Hariharan, P.C. and J.A. Pople, *The influence of polarization functions on molecular orbital hydrogenation energies.* Theoretical Chemistry Accounts: Theory, Computation, and Modeling (Theoretica Chimica Acta), 1973. **28**(3): p. 213-222.

32. Barone, V. and P. Cimino, *Accurate and feasible computations of structural and magnetic properties of large free radicals: The PBE0/N07D model.* Chemical Physics Letters, 2008. **454**(1-3): p. 139-143.

33. Barone, V., P. Cimino, and E. Stendardo, *Development and Validation of the B3LYP/N07D Computational Model for Structural Parameter and Magnetic Tensors of Large Free Radicals.* Journal of Chemical Theory and Computation, 2008. **4**(5): p. 751-764.

34. Adamo, C. and V. Barone, *Toward reliable density functional methods without adjustable parameters: The PBE0 model.* The Journal of Chemical Physics, 1999. **110**(13): p. 6158-6170.

35. Adamo, C., et al., *Tuning of Structural and Magnetic Properties of Nitronyl Nitroxides by the Environment. A Combined Experimental and Computational Study.* The Journal of Physical Chemistry A, 1999. **103**(18): p. 3481-3488.

36. di Matteo, A., et al., *Intrinsic and environmental effects in the physico-chemical properties of nitroxides. The case of 2-phenyl-4,4,5,5-tetramethyl-4,5-dihydro-1H-imidazol-1-oxyl 3-oxide.* Chemical Physics Letters, 1999. **310**(1-2): p. 159-165.

37. Barone, V., et al., *Assessment of a Combined QM/MM Approach for the Study of Large Nitroxide Systems in Vacuo and in Condensed Phases.* Journal of the

American Chemical Society, 1998. **120**(28): p. 7069-7078.

38.   Cirujeda, J., et al., *Spin Density Distribution of α-Nitronyl Aminoxyl Radicals from Experimental and ab Initio Calculated ESR Isotropic Hyperfine Coupling Constants.* Journal of the American Chemical Society, 2000. **122**(46): p. 11393-11405.

39.   Zheludev, A., et al., *Spin density in a nitronyl nitroxide free radical. Polarized neutron diffraction investigation and ab initio calculations.* Journal of the American Chemical Society, 1994. **116**(5): p. 2019-2027.

40.   Stipa, P., *A multi-step procedure for evaluating the EPR parameters of indolinonic aromatic aminoxyls: A combined DFT and spectroscopic study.* Chemical Physics, 2006. **323**(2-3): p. 501-510.

41.   http://www.ccdc.cam.ac.uk/.

42.   Frisch, M.J.T., G. W.; Schlegel, H. B.; Scuseria, G. E.; Robb, M. A.; Cheeseman, J. R.; Montgomery, J. A., Jr.; Vreven, T.; Kudin, K. N.; Burant, J. C.; Millam, J. M.; Iyengar, S. S.; Tomasi, J.; Barone, V.; Mennucci, B.; Cossi, M.; Scalmani, G.; Rega, N.; Petersson, G. A.; Nakatsuji, H.; Hada, M.; Ehara, M.; Toyota, K.; Fukuda, R.; Hasegawa, J.; Ishida, M.; Nakajima, T.; Honda, Y.; Kitao, O.; Nakai, H.; Klene, M.; Li, X.; Knox, J. E.; Hratchian, H. P.; Cross, J. B.; Bakken, V.; Adamo, C.; Jaramillo, J.; Gomperts, R.; Stratmann, R. E.; Yazyev, O.; Austin, A. J.; Cammi, R.; Pomelli, C.; Ochterski, J. W.; Ayala, P. Y.; Morokuma, K.; Voth, G. A.; Salvador, P.; Dannenberg, J. J.; Zakrzewski, V. G.; Dapprich, S.; Daniels, A. D.; Strain, M. C.; Farkas, O.; Malick, D. K.; Rabuck, A. D.; Raghavachari, K.; Foresman, J. B.; Ortiz, J. V.; Cui, Q.; Baboul, A. G.; Clifford, S.; Cioslowski, J.; Stefanov, B. B.; Liu, G.; Liashenko, A.; Piskorz, P.; Komaromi, I.; Martin, R. L.; Fox, D. J.; Keith, T.; Al-Laham, M. A.; Peng, C. Y.; Nanayakkara, A.; Challacombe, M.; Gill, P. M. W.; Johnson, B.; Chen, W.; Wong, M. W.; Gonzalez, C.; Pople, J. A., *Gaussian 03*, 2004, Gaussian, Inc.: Wallingford CT.

43.   Tomasi, J., B. Mennucci, and R. Cammi, *Quantum Mechanical Continuum Solvation Models.* Chemical Reviews, 2005. **105**(8): p. 2999-3094.

44.   Kusaba, Y., et al., *Isolation of crystals of a planar nitronyl nitroxide radical: 2-phenylbenzimidazol-1-yl N,N'-dioxide (PBIDO).* Journal of Materials

Chemistry, 1997. **7**(8): p. 1377-1382.

45. Stoll, S. and A. Schweiger, *EasySpin, a comprehensive software package for spectral simulation and analysis in EPR.* Journal of Magnetic Resonance, 2006. **178**(1): p. 42-55.

46. Peisach, W.B.M.a.J., ed. *Biological magnetic resonance*. ed. L.B.a.J. Reuben. Vol. 3. 1981, Plenum: New York.

47. Kevan, L. and R.N. Schwartz, *Time domain electron spin resonance*1979, New York: Wiley. viii, 414 p.

48. Hoff, A.J., *Advanced EPR : applications in biology and biochemistry*1989, Amsterdam ; New York New York, NY, U.S.A.: Elsevier; Distributors for the U.S. and Canada, Elsevier Science Pub. Co. xxii, 918 p.

49. Barone, V. and P. Cimino, *Validation of the B3LYP/N07D and PBE0/N07D Computational Models for the Calculation of Electronic g-Tensors.* Journal of Chemical Theory and Computation, 2008. **5**(1): p. 192-199.

50. Cheeseman, J.R., et al., *A comparison of models for calculating nuclear magnetic resonance shielding tensors.* The Journal of Chemical Physics, 1996. **104**(14): p. 5497-5509.

51. Koseki, S., M.W. Schmidt, and M.S. Gordon, *MCSCF/6-31G(d,p) calculations of one-electron spin-orbit coupling constants in diatomic molecules.* The Journal of Physical Chemistry, 1992. **96**(26): p. 10768-10772.

52. Mccracken, J., et al., *Pulsed Epr Studies of the Semiquinone State of Copper-Containing Amine Oxidases.* Journal of the American Chemical Society, 1992. **114**(10): p. 3715-3720.

53. Abdo el, M., et al., *Humoral and bronchial immune responses in cattle experimentally infected with Mycoplasma mycoides subsp. mycoides small colony type.* Vet Microbiol, 1998. **59**(2-3): p. 109-22.

54. Mims, W.B. and J. Peisach, *Nuclear Modulation Effect in Electron-Spin Echoes for Complexes of Cu2+ and Imidazole with N-14 and N-15.* Journal of Chemical

Physics, 1978. **69**(11): p. 4921-4930.

55.   Flanagan, H.L. and D.J. Singel, *Analysis of N-14 Eseem Patterns of Randomly Oriented Solids.* Journal of Chemical Physics, 1987. **87**(10): p. 5606-5616.

56.   Lucken, E.A.C., *Nuclear quadrupole coupling constants*1969, London, New York,: Academic Press, 360 p.

57.   Hurst, G.G., T.A. Henderson, and R.W. Kreilick, *Angle-selected ENDOR spectroscopy. 1. Theoretical interpretation of ENDOR shifts from randomly orientated transition-metal complexes.* Journal of the American Chemical Society, 1985. **107**(25): p. 7294-7299.

58.   Pople, J.A., M. Headgordon, and K. Raghavachari, *Quadratic Configuration-Interaction - a General Technique for Determining Electron Correlation Energies.* Journal of Chemical Physics, 1987. **87**(10): p. 5968-5975.

59.   Moreno-Armenta, M.G. and A.L. Cooksy, *Ab initio study of the cyclooctatetraenyl radical.* Journal of Physical Chemistry A, 2005. **109**(15): p. 3391-3395.